

Design of a Fatigue-Resistant Shape Memory Alloy for Artificial Heart Valve Frames

This entry is based on a team project that was conducted for the following course:
Materials Science and Engineering 390 - Materials Design

Faculty Advisor: Professor G.B. Olson
Graduate Student Advisor: Dana Frankel

Ryan DeBlock
Kelsey Jorgensen
Cheyenne Lynsky
Edward Pang
Sarah Plain
Peter Santos
Rachel Wang

Northwestern University
Robert R. McCormick School of Engineering and Applied Science
Department of Materials Science and Engineering

Department of Materials Science and Engineering
Northwestern University
2220 Campus Drive
Cook Hall Room 2036
Evanston, IL 60208-3108

June 14, 2014

Contents

1	Scientific Background	4
1.1	Motivation	4
1.2	Shape Memory and Superelasticity	4
1.3	Discovery of Shape Memory Alloys and NiTi	6
1.4	Processing Methods	6
1.5	Fatigue	7
1.6	Strengthening	7
1.6.1	Cold Working	8
1.6.2	Precipitation Strengthening	8
1.7	Biocompatibility	10
2	Team Organization (RAM)	10
2.1	RAM	10
2.2	Assignment Justification	11
2.2.1	Alloy Design	11
2.2.2	Strength Modeling	11
2.2.3	Coarsening Model	11
2.2.4	Processing Options	11
3	Property Objectives (CES)	12
3.1	Strengthening	12
3.2	Fatigue Resistance	12
3.3	Transformation Temperature and Superelasticity	12
3.4	Radiopacity	12
4	Design Approaches	13
4.1	Systems Approach	13
4.2	System Structure	14
4.3	Design Steps	15
4.4	Processing	16
4.5	Strengthening	16
4.5.1	Solid Solution Strengthening	16
4.5.2	Precipitation Strengthening	17
4.6	Precipitate Shear Resistance	18
4.6.1	Modulus Hardening	18
4.6.2	Other Strengthening Contributions	18
4.7	Orowan Looping	19

4.7.1	Incipient Melting	19
4.8	DFT Simulations for Precipitate Strengthening	20
4.8.1	Background to DFT Simulations	20
4.9	Aging Treatment	20
4.9.1	Misfit	23
4.9.2	Modeling Software	23
4.10	Transformation Temperature	24
4.11	Radiopacity	24
5	Powder Metallurgy	25
5.1	Mechanical Alloying	25
5.2	Sintering Methods	26
5.3	Gettering of Oxygen	26
6	Results	27
6.1	DFT Calculations	27
6.1.1	DFT Calculation Approach	27
6.2	K1 Model and Capillary Energy Determination	33
6.3	Final Alloy Design	35
7	Conclusions	39

1 Scientific Background

1.1 Motivation

NiTi, often called nitinol, is a shape memory alloy (SMA) that has been of great interest for medical applications, ranging from wires in the orthodontic field to staples and plates in the orthopedic field to coils, stents and micro-guide-wires in the neurosurgical field [1]. However, the most promising and pressing motivation for research in shape memory alloys is in the vascular field. The heart is one of the most important organs in our body. It is a muscle essential to our survival. The heart beats around 72 times per minute, pumping blood throughout our body. Interruptions to the continuous function of the heart is a serious problem that can be life threatening. In order to last 30 years before failure, the heart valve or stent must survive 1.14 billion cycles. This underscores the need for good fatigue performance into the ultra-high cycle fatigue (UHCF) region.

The venous “Simon filter” is one of the first applications of SMAs in the vascular field. It functions as a device that prevents blood clots in patients who are unable to tolerate anticoagulants. When made, the device is in its expanded shape and in the martensitic phase. The martensite phase is a metastable crystal structure at room temperature. The device is then crimped onto the catheter, which induces a transformation from multi-variant to single variant martensite, allowing the ease of insertion into the catheter. Upon placement in the body, the increase in temperature causes the martensite-austenite transformation for the device to return to its original shape, to function as a preventer of blood clots in the blood stream [2]. While the “Simon filter” takes advantage of nitinol’s shape memory property, similar filters utilize its super-elastic property, in which the open configuration is in a stable austenitic phase. The device is then crimped and upon insertion to the body recovers to the original shape due to superelasticity [3]. Other than filters, a variety of nets and stents made from SMAs are used to respectively close ventricular septal defects and restore blood stream to peripheral tissues [4, 5].

The clear benefit of SMA devices lies in their ease of insertion and the possibility of minimally invasive techniques in favor of traditional surgical methods. This leads to interest in SMA applications in relation to heart valve diseases. The heart consists of four valves including the mitral, aortic, tricuspid and pulmonary valves which together regulate the flow of blood throughout the heart’s four chambers. Per heartbeat, the valves simultaneously open to allow blood flow to the subsequent chamber and close preventing backflow. Heart valves can fail in two main ways, regurgitation or stenosis. Regurgitation occurs when the valves do not completely close, allowing backflow and leakage of blood in reverse. Stenosis occurs in which the valves stiffen and do not completely open, creating blockage and limiting blood flow [6]. Traditional surgical valve replacements, either artificial or biological prostheses, require a thoracotomy, an open-heart surgery that has significant risks. With shape memory alloys, a percutaneous method is possible in which the valve can be inserted through the femoral artery, which allows for a much lower surgical risk. In addition, the patients require fewer blood transfusions and experience less post-operation pain. The recovery is faster and therefore hospital stays are shortened [7].

1.2 Shape Memory and Superelasticity

Shape memory alloys are materials that can be deformed from a preset orientation, but return to that original shape with the application of heat. The stress-strain characteristics of this phenomenon are shown in Figure 1.

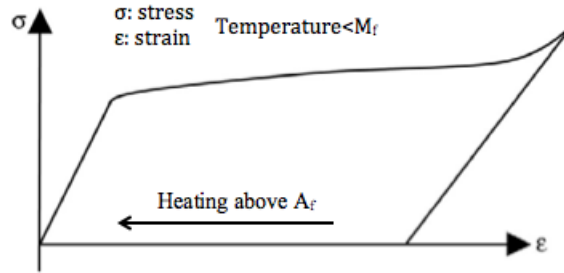


Figure 1: Stress strain curve of the shape memory effect. The material can be plastically deformed (following the pattern on the curve), and upon heating above the austenite transformation temperature the material will return to its original orientation [8].

This is accomplished through a series of phase transformations. In NiTi, the most common shape memory alloy, the relevant phases are a strong austenitic phase and a weak martensitic phase. The highly-symmetric cubic crystal structure of the austenitic phase (ordered BCC or B2) allows it to only take on a single orientation, while the low-symmetry martensitic phase can exist in several variants (up to 24 unique crystal variants for monoclinic B19' martensite). At high temperatures the austenite phase can be deformed into a new “remembered shape,” and then cooled below the martensitic transformation temperature. Deformation of the martensite occurs via a reversible twinning process in which variants are reoriented to produce accommodation strain in response to mechanical loading. However, when heated back above the austenite transformation temperature, the crystal will return to the austenite phase and “remember” its previous shape. If the martensite is deformed so much that it can no longer reorient itself to accommodate strain, plastic deformation will occur and the previous shape will not be remembered upon heating.

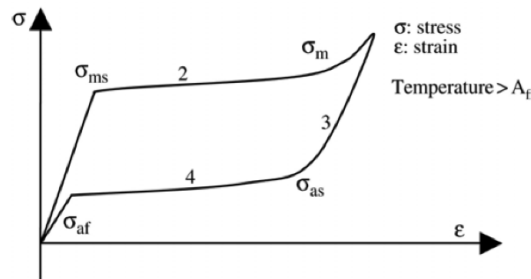


Figure 2: Stress strain curve of a superelastic alloy. The material can be elastically strained, but at (2) the material undergoes a phase transformation to the martensite phase which allows a different mode of deformation. At (3) the loading is relaxed, and at (4) the material transforms back into the austenitic phase to regain its original shape without any plastic deformation [8].

Superelastic behavior is shown in Figure 2. Superelasticity is a phenomenon very similar to the shape memory effect, but does not require temperature changes. Instead, when a superelastic alloy undergoes considerable stress, a martensitic phase transformation occurs which allows the material to strain. During this transformation the martensitic variants align along the loading axis so that a large strain is observed without a change in stress. However, when the strain is released the material undergoes a reverse phase transformation from martensite to austenite, and the materials can then return to its original shape. Alloys with this property can undergo very high, reversible strains (up to 8.5%) without undergoing any plastic deformation, thus allowing for full strain recovery during unloading [9].

1.3 Discovery of Shape Memory Alloys and NiTi

Shape memory alloys were first discovered in 1932 by Arne Ölander in the gold-cadmium system. Six years later, Greninger and Mooradian documented shape memory effects in copper zinc alloys as well [10]. However, these materials remained scientific curiosities until nitinol was developed in 1962. Nitinol, which stands for “Nickel Titanium Naval Ordinance Laboratories,” was accidentally discovered when Dr. David S. Muzzey, a technical director, heated a deformed sample with his pipe lighter [11]. This discovery prompted research into the nickel-titanium system and the subsequent implementation of nitinol into the market. Several applications include: retractable antennas, actuators, sporting goods, glasses frames, and toys [9]. Moreover, nitinol’s shape memory and superelastic properties make it an ideal material for biomedical applications.

1.4 Processing Methods

The current manufacturing processes for commercial NiTi products include vacuum induction melting (VIM), vacuum arc remelting (VAR), or a hybrid process where samples prepared by VIM are further refined using a VAR process. These melting techniques are of particular interest due to the detrimental effects of non-metallic inclusions that are introduced into the alloy during processing [12]. Virtually all of these inclusions form within the alloy during solidification or subsequent processing steps. Studies have shown that these inclusions are typically carbides (TiC) and oxides ($Ti_4Ni_2O_x$) [13]. In VIM processing, Ni pellets and Ti rods are melted within a graphite crucible under a vacuum or inert gas atmosphere. During melting, a small amount of carbon diffuses into the melt, which later forms TiC carbides during solidification. One step that can be taken to reduce carbon content in the melt is to use Ti disk cladding to reduce Ni contact with the crucible. This cladding forms a protective TiC coating on the inside surface of the crucible, but it does not completely inhibit the transfer of carbon into the melt [14]. A schematic of this process is shown in Figure 3.

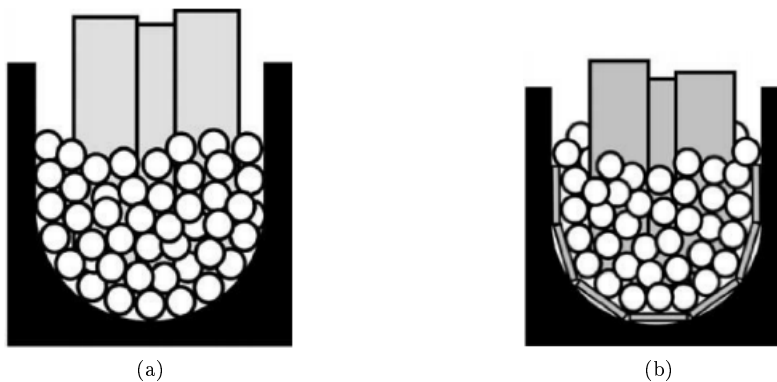


Figure 3: Schematic of the VIM process with (a) full contact of Ni pellets with the graphite crucible and (b) Ti disk cladding to prevent direct contact between the Ni and graphite [14].

During VAR processing, a consumable electrode of the materials to be melted is used rather than a crucible. This has significantly lower carbon content than the VIM method, but some oxygen pick up still occurs [14]. These processes, along with the purity of the raw materials used, determine the purity of the end product. Comparisons of these methods shows that VIM ingots contain approximately 300-700 ppm of carbon, and VAR ingots contain less than 100 ppm of carbon. Both have shown typical oxygen content of roughly 300 ppm [15]. While the inclusion concentration is higher in VIM ingots, the advantage to this process is composition control; if the process is done carefully, the M_s temperature can be controlled to within $\pm 5^\circ C$ [14].

The morphology of the inclusions can be significantly changed during post-processing. After solidification, wire or tube drawing is required in order to make stents or other small components. The large internal stresses caused by these cold working processes can subsequently fracture and separate inclusion particles

[13]. In general, carbide or oxide inclusions larger than $9\mu\text{m}$ in diameter will break up in this fashion and form what are known as stringers (Figure 4). After standard VIM and VAR processing, oxides tend to have a larger average size and a maximum size of roughly $30\mu\text{m}$ [13]. Due to this trend, most stringers formed during cold working originate from large oxide inclusions. Stringers can reach up to $100\mu\text{m}$ in length, and often contain voids where the matrix and the inclusions have separated. This is particularly detrimental to fatigue life due to the high potency of the voids as crack nucleation sites [13].

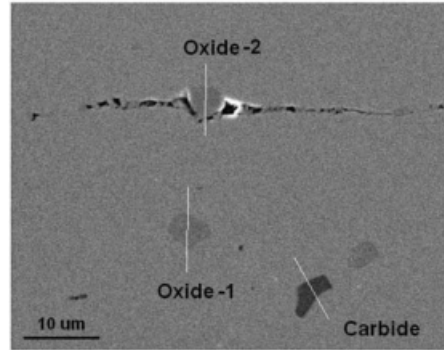


Figure 4: Backscatter SEM image containing both isolated carbide and oxide inclusions as well as an oxide stringer [13].

Another problem posed by the presence of inclusions is their effect on the local composition of the matrix. The goal is to have roughly a 1:1 ratio of Ni to Ti, but inclusions deplete the matrix of Ti. This can strongly affect the transformation temperature, because an increase in the Ni content of 0.1 at% can decrease the transformation temperature by 10°C [16].

1.5 Fatigue

As mentioned above, inclusions from processing can negatively impact the fatigue lifetime of NiTi by providing sites for the nucleation and propagation of fatigue cracks over many cycles. Fatigue is the change or degradation of material properties through thermal or mechanical cyclic loading. The alloy intended for biomedical applications in this design proposal will mainly experience mechanical cycling through blood vessel dilation and contraction. Thermal cycling will be assumed to be negligible due to limited fluctuations in body temperature.

The fatigue experienced by shape memory alloys can be categorized as either functional fatigue or structural fatigue. These both originate from the accumulation of small amounts of slip deformation, which accommodates the martensitic transformation [17]. Functional fatigue regards the loss of the functionality of the nitinol as a shape memory alloy and a superelastic material. Structural fatigue compromises the structural integrity of a material through the accumulation of damage that can propagate voids and ultimately cracks. This is the same type of fatigue typically considered for non-shape memory alloys, but the NiTi alloys will behave differently under different temperature ranges. Each time the material transforms, localized stress concentrations exist on the edges of the martensite plates. If the matrix is not strong enough, accommodation slip dislocations are introduced in the material and produce localized plasticity [18]. This leads to cyclic instability and a lower fatigue life as dislocations pile up, also resulting in a significant amount of irreversible strain during each transformation cycle. In addition to irreversible strain, the transformation stress (σ_{M_s}) also decreases making strain recovery more difficult.

1.6 Strengthening

Biomedical uses of NiTi alloys demand exceptional mechanical fatigue life in the ultra-high cycle regime. Thus, increasing the flow stress of the B2 austenite phase is a priority to achieve stable cyclic performance

and superior fatigue life by minimizing the amount of accommodation slip. Figure 5 shows the effects of B2 strengthening on the material cyclic performance in pure NiTi. An increase in B2 flow stress from 737 MPa to 1360 MPa produces much less permanent strain between cycles and an improvement in cyclic stability. It is thus apparent that strengthening of the matrix promotes reversible twinning and detwinning instead of irreversible plastic deformation [18].

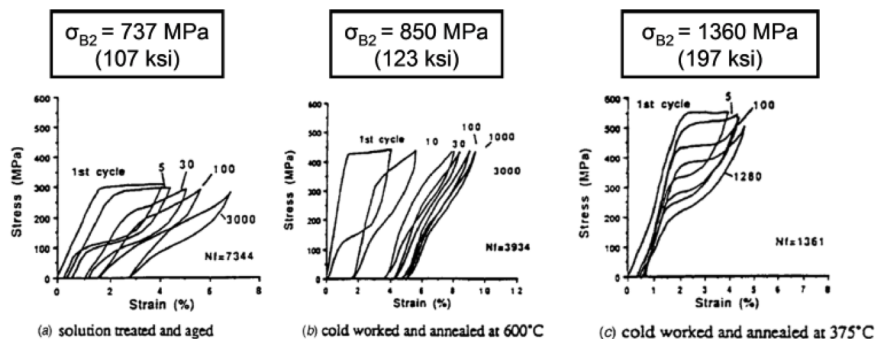


Figure 5: Stress-strain cycles for pure NiTi. An increase in cyclic stability (permanent strain between cycles) can be observed with an increase in B2 matrix phase flow stress[19].

1.6.1 Cold Working

Many NiTi alloys to date are strengthened by cold working [18, 15]. However, this process results in the formation of inclusion stringers and greatly increases the dislocation density, both of which can severely compromise the material’s fatigue life.

Cold worked NiTi has been shown to have a slightly higher strength than precipitation-strengthened binary NiTi; however, it is apparent that precipitation-strengthened NiTi possesses far superior cyclic stability (Figure 6) [20]. A precipitation-strengthened approach to increasing the B2 phase flow stress is thus desired.

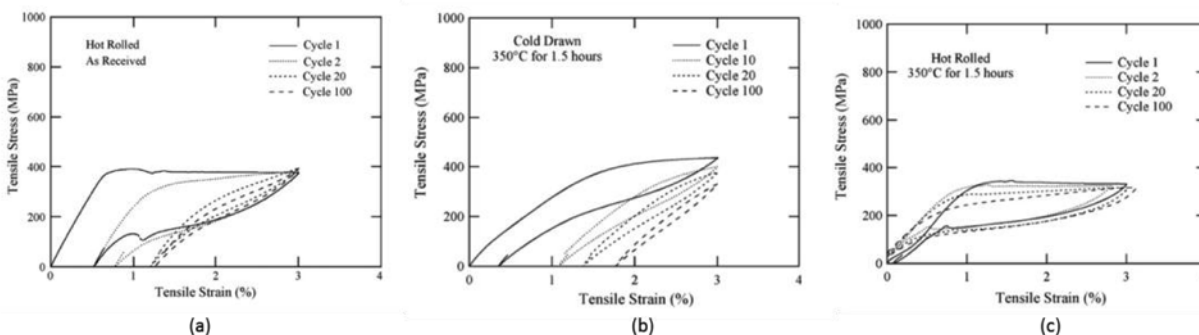


Figure 6: Stress-strain curves for superelastic cycling in NiTi. (a) Annealed .(b) Cold worked and aged (no precipitates observed). (c) Hot rolled and aged (precipitates observed) [20].

1.6.2 Precipitation Strengthening

One strengthening method in the literature involves a metastable BCT phase, but this has only been achieved during the annealing of sputter-deposited NiTi thin films [21]. The more promising method is the precipitation of equilibrium Ni₂TiAl (Heusler phase) with an L₂₁ structure (Figure 7). Similar to the precedent of the nickel-based superalloys (fcc-based γ/γ'), the L₂₁ is a further ordered form of the B2 structure [21].

Heusler phase precipitation strengthening has been demonstrated to increase the compressive yield strength of a $\text{Ni}_{50.71}\text{-Ti}_{40.86}\text{-Al}_{8.43}$ (in at%) alloy by an order of magnitude to 2300 MPa [22].

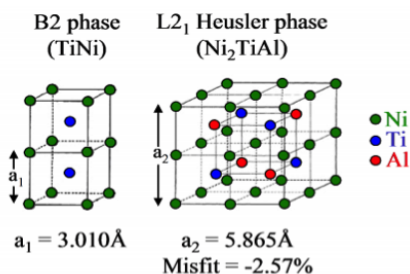


Figure 7: Matrix B2 crystal structure (left) and L₂₁ Heusler phase precipitate crystal structure [23].

The L₂₁ precipitate structure is coherent with the B2 matrix structure, with a lattice misfit of -0.0257 in the NiTiAl system [21]. However, to encourage homogeneous nucleation of fine precipitates, maintain precipitate coherency, and promote martensite nucleation and variant growth, coherency strains must be minimized. Therefore, Heusler phase strengthening necessitates the addition of large alloying constituents such as Hf, Pd, Pt, and Zr to substitute in the L₂₁ structure. Hf, Pd, Pt, and Zr are common martensite stabilizers and have been previously used as additions to NiTiAl alloys [21]. Previous empirical studies have been done to show that adding 8.4 wt% Al to a NiTi lattice can create a coherent Ni₂TiAl Heusler phase that raised the yield strength to 2.3 GPa, however these results lack the controls on particle size and phase fraction which will be needed to create a comprehensive strength model [22].

Bender et al. designed a Ni₂₀Pd₃₀Ti₄₆Al₄ Heusler phase-strengthened superelastic alloy to demonstrate the effectiveness of this method [18]. DSC traces in Figure 8 compare the thermal cyclic stability of pure NiTi versus the newly developed Heusler phase-strengthened alloy. Whereas the pure NiTi exhibits a shift of 10°C in its transformation behavior within the first 30 cycles, aged Ni₂₀Pd₃₀Ti₄₆Al₄ demonstrates complete thermal stability. Figure 9 compares the mechanical cyclic stability of the same two alloys. The permanent strain is decreased from 0.6% in pure NiTi to less than 0.2% in the Ni₂₀Pd₃₀Ti₄₆Al₄ alloy while the stress hysteresis greatly decreases from 516 MPa in pure NiTi to 113 MPa in the Ni₂₀Pd₃₀Ti₄₆Al₄ alloy. However, the Ni₂₀Pd₃₀Ti₄₆Al₄ alloy possesses a considerably lower transformation strain.

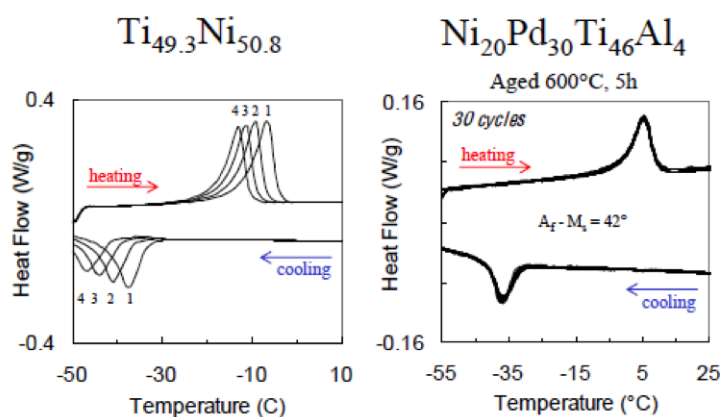


Figure 8: Thermal cyclic stability comparison between pure NiTi and aged Ni₂₀Pd₃₀Ti₄₆Al₄ alloy [18].

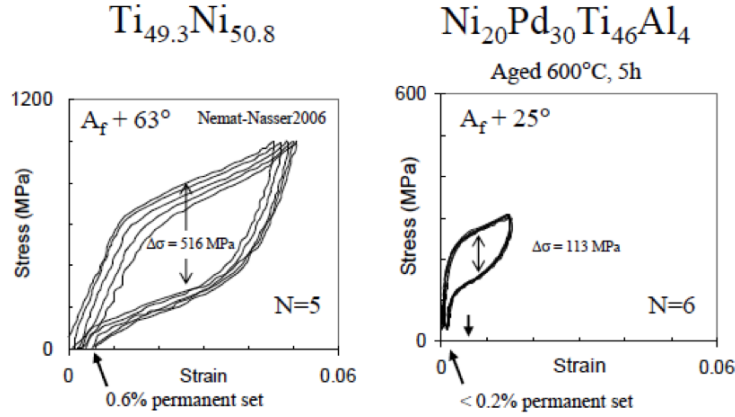


Figure 9: Mechanical cyclic stability comparison between pure NiTi and aged Ni₂₀Pd₃₀Ti₄₆Al₄ alloy [18].

1.7 Biocompatibility

The use of SMAs in biomedical applications raises concerns about biocompatibility and highlights the need for the material to be nontoxic, nonthrombogenic, noncarcinogenic, nonantigenic and nonmutagenic. Specifically for a heart valve, the material needs to have blood compatibility and nonthrombogenicity so that blood clots do not form [24, 25].

Extensive studies have been conducted on the biocompatibility of NiTi shape memory alloys used for medical applications. Research has focused on corrosion properties, in vitro and in vivo biocompatibility, and the release of Ni ions. NiTi SMAs have been shown to possess good corrosion resistance and low cytotoxicity in vitro and in vivo, provided the material is anodized to form a protective TiO₂ layer. In fact, anodized NiTi can be more corrosion resistant than conventional implant materials such as stainless steel [24].

The main biocompatibility concern with NiTi results from the high nickel content in equiatomic NiTi alloys. A significant portion of the population, 8 to 20 percent of females, is allergic to trace quantities of nickel, and above the recommended daily intake threshold, nickel is toxic and carcinogenic [26]. In reality, however, titanium is much more readily oxidized than nickel. This allows NiTi to form a protective TiO₂ surface layer that limits the concentration of nickel that can diffuse into the body to under recommended daily intake values. With the consideration of biocompatibility, our first design (referred to as the “hybrid”) will focus on the (Ni,Pd)₅₀(Ti,Zr,Al)₅₀ system, with the substitution of palladium to lower the overall nickel content.

2 Team Organization (RAM)

2.1 RAM

	R. D.	C. L.	S. P.	E. P.	K. J.	P. S.	R. W.
Alloy Design							
Strengthening model/ DFT							
Coarsening Model							
Powder Metallurgy							

The team is coached and advised by Dana Frankel, a fourth-year Ph.D. candidate in materials science and engineering. Dana’s research is centered around designing shape memory alloys for heart valve applications, making her uniquely qualified to advise the team. The rest of the team, which is composed of undergraduates in materials science and engineering at Northwestern University, are: Ryan DeBlock, Kelsey Jorgensen,

Cheyenne Lynsky, Edward Pang, Sarah Plain, Peter Santos, and Rachel Wang. The RAM chart above represents the primary and secondary assignments of each team member, respectively. Moreover, Dr. Wei-Wei Zhang and Dr. Wei Xiong have provided additional technical advising to the team. Further description of roles is provided in Section 2.3.

2.2 Assignment Justification

2.2.1 Alloy Design

Ryan and Edward will take a primary role in alloy design of the hybrid alloy. Rachel, Kelsey, and Cheyenne will have a secondary role in assisting with this task.

Kelsey and Cheyenne will bring their knowledge of fatigue and strengthening mechanisms gained through courses taken at Northwestern University to this subgroup.

Rachel will use her experience gained through working at Phillips Electronics, where she analyzed Ti-Zr-Mo alloys used in x-ray targets.

Ryan will utilize his experience in MATLAB in order to coordinate the output from the other subgroups. In addition, his role at GE Aviation dealt with the detection of voids/cracks in metals and composites and he hopes to bring his knowledge to this team. He is also interested in the effects that precipitation strengthening will have on the overall performance of the hybrid alloy.

Edward has prior research experience with superelastic NiTi at NASA Glenn Research Center, working with Malcolm Stanford, Chris Dellacorte, and Ron Noebe. He studied the rolling contact fatigue properties of ball bearing components being designed for the International Space Station and worked to develop new compositions and heat treatments to improve strength and fatigue life. His knowledge of the Ni-Ti system will allow him to play an effective integration role in alloy design.

2.2.2 Strength Modeling

Peter will take the lead on the DFT calculations to further understand the strengthening dispersion of the alloy. His research on organic photovoltaics has given him experience in rudimentary molecular modeling, making him well prepared to work on DFT modeling. Additionally, Wei is an expert in DFT and will be able to provide guidance and training for this portion of the project.

Edward conducts research with Dr. Dunand and Dr. Seidman on high-temperature aluminum, primarily focused on nano-scale precipitation strengthening. He also writes computational simulation codes with Dr. Voorhees to study crystallization in thin film conducting oxides. His background in precipitation strengthening and computational simulations will be an asset in these roles.

2.2.3 Coarsening Model

Cheyenne will take on the primary role of calculating the precipitation kinetics of phase transformations using the Lee Coarsening Model. Cheyenne has little prior knowledge of this model but has experience with mobility and other kinetic calculations. This background and an interest in the precipitation strengthening of materials will allow her to be a strong contributor to this role. Kelsey will have a secondary role on this task.

2.2.4 Processing Options

Sarah will assume the primary role in researching alternative processing methods. Her experience working with GE Aviation has sparked her interest in how manufacturing methods affect the final properties and performance of materials. While working at GE, her first project involved researching alternative corrosion

protection coatings to replace the hazardous hexavalent chromium coatings used on many aviation parts. She hopes to apply her research experience to find an efficient alternative processing technique for NiTi to improve its ability to function as a medical device. Rachel will have a secondary role on this task.

3 Property Objectives (CES)

3.1 Strengthening

Properly functioning heart valves are vital to the health of humans; therefore, the tolerance for failure in their artificial counterparts is extremely low. Developing a comprehensive strength model will allow for the design of an alloy with a yield strength above 2 GPa so that transformation strain will be accommodated elastically, minimizing slip and ultimately increasing fatigue lifetime. Strengthening should be achieved without increasing dislocation density [27].

3.2 Fatigue Resistance

A primary requirement for this alloy design is fatigue resistance. The biomedical service applications of this alloy demand ultra-high cycle fatigue resistance in the billion cycle range to accommodate the dilation and contraction of blood vessels and heart valves. While improving austenite strength is critical in improving fatigue resistance, oxide and carbide precipitates act as nucleation sites for voids and cracks, ultimately reducing the cyclic lifetime of the alloy. Various processing techniques will be explored to minimize the deleterious effects of non-metallic inclusions. The objective is to achieve at least a 50% increase in the allowable strain amplitude relative to current NiTi alloys.

3.3 Transformation Temperature and Superelasticity

In order to ensure the alloy will be used in its superelastic form, the transformation temperature must be controlled so that it is below the use temperature of a device. In biomedical applications this will be human body temperature (37°C). An austenite finish temperature (Af) of 10°C-15°C gives a wide margin to ensure that the use temperature is always above Af so that the material behaves superelastically.

Superelasticity and shape-memory are highly-desired material properties in biomedical applications. Stents, implants, and other medical devices can be introduced into the body in a small, minimally invasive form. Upon heating to body temperature, the part will assume its designed shape and behave superelastically. In use, the superelastic characteristic of the material allows it to be exposed to high amounts of strain without permanently deforming.

3.4 Radiopacity

Radiopacity refers to the inability of light (in this case X-rays) to pass through a material. Shape memory alloy stents and heart valves can be implanted in a minimally invasive procedure as opposed to open heart surgery. Devices are inserted via catheter under X-ray fluoroscopy to ensure proper placement. Radiopacity is measured with a mass attenuation coefficient (μ/ρ) where μ is the attenuation coefficient and ρ is the density of the material. The transmission of X-rays through a material can be described by:

$$I = I_o \exp\left(-\frac{\mu}{\rho} * \rho x\right)$$

where x is the material thickness [18]. The mass attenuation coefficient for pure NiTi at 30 keV is 7.93 [18]. The designed alloys should have a greater mass attenuation coefficient than pure NiTi [28].

Table 1: Summation of the property objectives for this design project.

Property	Design Objective
Transformation Temperature	$A_f = 10^\circ \text{C} - 15^\circ \text{C}$
Yield Strength	$\geq 2 \text{ GPa}$
Misfit	$\leq 1\%$
X-Ray Absorption (μ/ρ)	> 8.0

4 Design Approaches

4.1 Systems Approach

Traditionally, the development of materials has largely been based on experimentation. Empirical results would be correlated with known properties, followed by continuous modifications and improvements through iterative design. In addition to being ineffective in creating significant improvements, this process is also time consuming and costly. The technology improvements of the 21st century has allowed for the development of computational methods, which can serve to greatly accelerate the materials design process. From basic understanding of materials science and increasingly expanding databases for materials, computations can be done to predict a material’s structure and properties. This fast-tracks development of an optimal material as it eliminates the need to recreate the materials with each modification to the design.

Nevertheless, materials are complex by nature. Jenkins introduces a systems approach, which breaks down the complex problem into groups of interacting subsystems of problems [29]. Although broken down, the system optimization is still done as a whole; it incorporates an “overall approach” to achieve an “overall objective.” The main steps in the systems approach include systems analysis, system design or synthesis, implementation, operation and improved operation. System analysis introduces an overview of the organization of the project and provides a definition of the problem, objectives, and data required. System design involves the building of a quantitative model to serve as a tool to predict and simulate how the system would operate under various conditions, which is essentially the key optimization process.

Cyril Smith was the first to apply the systems approach to materials science [30]. He recognized the complexity of materials and treated them as an interactive structural hierarchy of subsystems.

Olson has taken the ideas of Smith and Jenkins and applied them to materials design, emphasizing the importance of the processing-structure-properties-performance relationship shown in Figure 10 [31, 32]. The traditional scientific approach utilized by materials scientist utilizes a workflow from left to right, seeking to understand how processing affects structure, which properties arise from the given structure, and how the properties define materials performance. However, a materials engineer is interested in the reverse workflow, where the most important aspect of a material is its performance. This drives property requirements, the structures required to achieve these properties, and finally which processing routes can achieve the necessary structures.

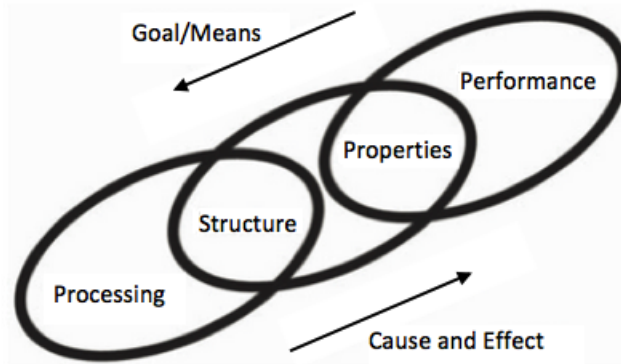


Figure 10: Three-link chain model of the central paradigm of materials science and engineering[32].

4.2 System Structure

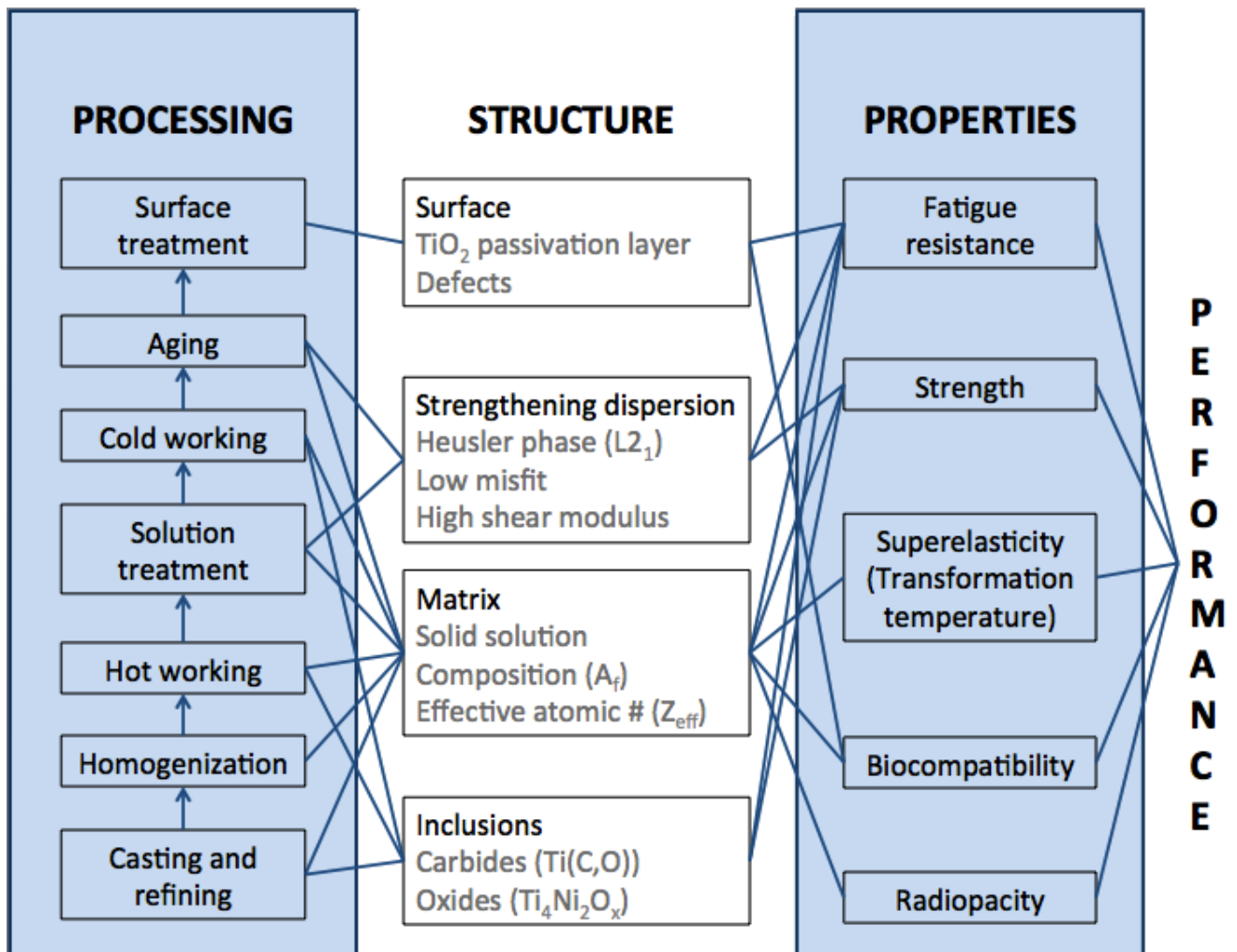


Figure 11: System chart depicting the relations between processing, structure, properties, and performance of a superelastic material for biomedical applications.

Our system structure for designing a superelastic material for biomedical applications is shown above in Figure 11. This chart visually demonstrates the processing, structure, and property relations that we will be considering to design a material with the desired performance characteristics. Properties of particular importance include fatigue resistance and superelasticity (controlled by the transformation temperature). These properties must meet minimum requirements outlined in the previous section to ensure safe operation. A large focus on material structure will center on the strengthening dispersion of Heusler $L2_1$ phase precipitates, which in turn strongly depends on the solution treatment and aging process designs.

4.3 Design Steps

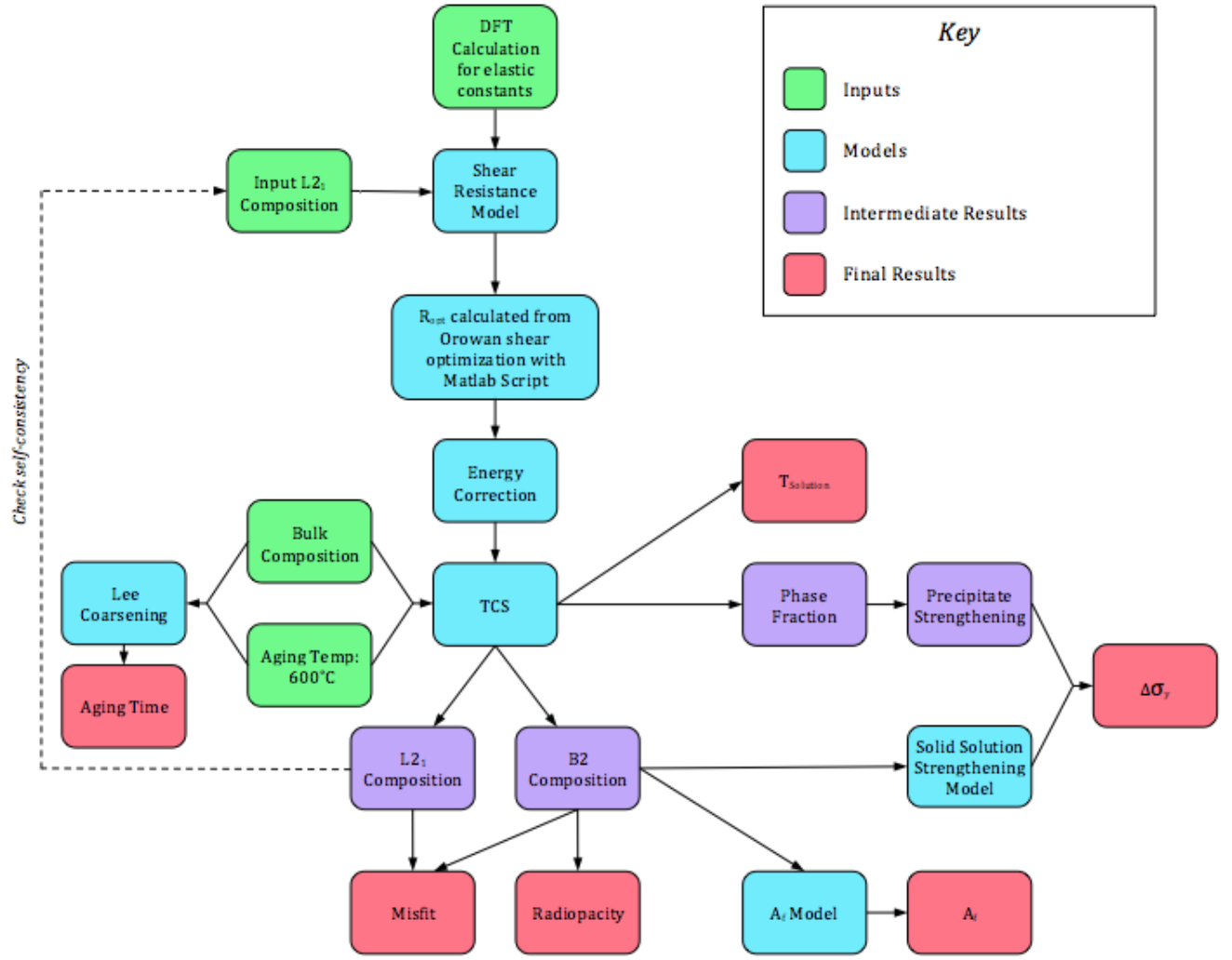


Figure 12: Flow Chart for the design approach used

The project goal includes the design of an alloy that fit the property objectives. The alloy design focuses on a lower Ni content in an effort to increase biocompatibility.

The models used in this design are summarized in Table 2:

Table 2: Description of the main property objectives and the models and experimental techniques required to obtain these properties.

Property	Model	Experimental Technique
Transformation temperature	Redlich-Kister	DSC
Precipitate shear resistance	Precipitation strengthening model ($\Delta\sigma_{ppt}$)	Hardness testing, DFT
Solid solution strength	Solution strengthening model ($\Delta\sigma_{ss}$)	Hardness testing
Misfit	Misfit model	Theoretical atomic radii, XRD
Absorption	Radiopacity model	X-ray fluoroscopy

4.4 Processing

There is interest in researching alternative processes to replace VIM/VAR NiTi alloys that involve expensive thermomechanical treatments and subsequent subtractive processing through machining. As previously stated, cold working is often involved in strengthening melt-processed NiTi. This causes the formation of stringers from oxide and carbide inclusions, which act as potent crack nucleation sites that drastically reduce fatigue life. A promising alternative process is the fabrication of NiTi via powder metallurgy, particularly for compositions prone to high solidification microsegregation. A literature review has been conducted to gather information about the potential of powder metallurgy to provide a more economical processing method while also improving the properties of NiTi SMAs traditionally fabricated by VIM and VAR.

4.5 Strengthening

4.5.1 Solid Solution Strengthening

The addition of alloying elements which substitute on B2 matrix lattice sites provides a source of strengthening. These atoms possess a different atomic radius than the host Ni or Ti atoms and thus cause a local stress field as the crystal structure is distorted. These stress fields interact with dislocations moving through the crystal and impede their motion, contributing to strengthening of the material.

The theoretical solid solution strengthening model is as follows [33]:

$$\Delta\sigma_i = k_i X_i^{1/2}$$

where k_i is the strengthening constant for solute i and X_i is the mole fraction of solute i . Jung measured the strengthening constants in NiTi to be 2575 MPa for Al and 2730 MPa for Zr [34]. Palladium has been shown to be a solution softener, but the $\frac{1}{2}$ power dependence in the standard solution strengthening model above is unproven for solution softeners [35]. Therefore, Jung assumed a linear dependence on palladium concentration with a “strengthening constant” of -347 MPa. The total solution strengthening model is thus as follows:

$$\Delta\sigma_{ss} = (2575MPa) X_{Al}^{1/2} + (2730MPa) X_{Zr}^{1/2} - (347MPa) X_{Pd}$$

4.5.2 Precipitation Strengthening

Precipitation Strengthening vs. Precipitate Radius

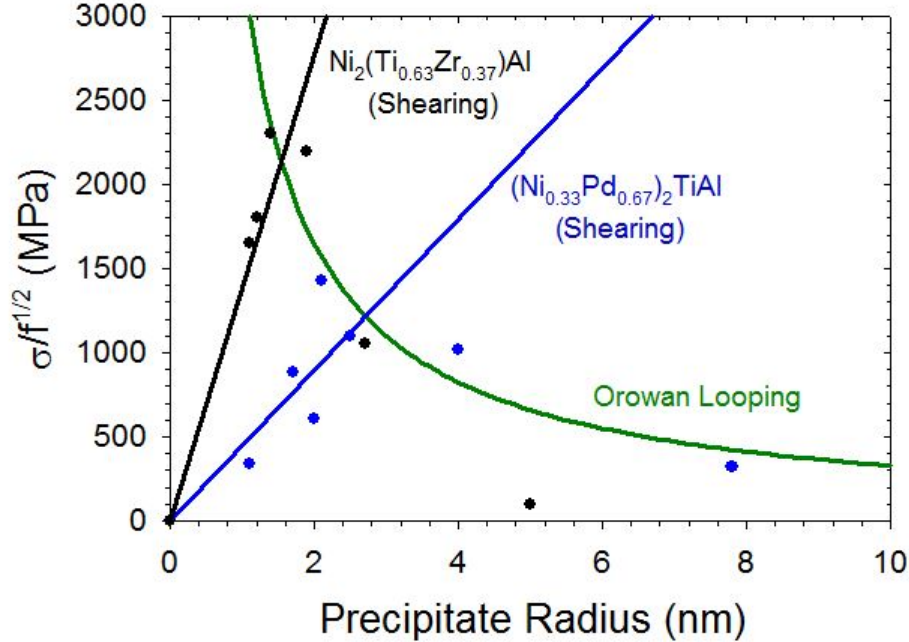


Figure 13: Precipitation shear strengthening (normalized by volume fraction) and Orowan strengthening versus precipitate radius for $\text{Ni}_2(\text{Ti}_{0.63}\text{Zr}_{0.37})\text{Al}$ and $(\text{Ni}_{0.33}\text{Pd}_{0.67})_2\text{TiAl}$ [36]. The precipitate size resulting in maximum strengthening occurs at the intersection between the two modes of strengthening. Greater K_1 (slope of precipitate shear strengthening vs. radius) result in greater strengthening potential at lower precipitate radii [37, 23].

When a dislocation moving through the matrix meets a precipitate, two competing mechanisms describe the precipitate-dislocation interaction: 1) Precipitate shearing, which occurs when the dislocation shears through the precipitate, and 2) Orowan Looping, which occurs when the dislocation bows and generates a new dislocation (Frank-Read source) which continues moving through the matrix.

The two models used for the two domains are:

$$\text{Precipitate Shearing: } \Delta\sigma_{ppt, shear} = K_1 f^{1/2} r$$

$$\text{Orowan Looping: } \Delta\sigma_{ppt, Orowan} = K_2 \frac{f^{1/2}}{r}$$

It is important to note that the classical $r^{1/2}$ dependence of precipitate shearing contributions to strength was not used. Experimental data appears to suggest a linear relation between precipitate shear strengthening and precipitate radius (see Figure 13).

For the alloy, a K_1 model was used to predict shear resistance of a hybrid precipitate in a 2-D design space (varying at% Pd and at% Zr).

4.6 Precipitate Shear Resistance

The coherent nature of the L2₁ precipitates in a B2 matrix favor a precipitate shearing mechanism at small precipitate radii. Our alloy design seeks to improve precipitate shear resistance primarily through modulus hardening.

4.6.1 Modulus Hardening

When a dislocation enters a precipitate with a shear modulus different from that of the matrix, the line tension inside the precipitate is altered, which impedes movement of the dislocation through the precipitate [38]. Melander and Persson developed a quantitative model for the contribution of modulus mismatch strengthening [39]. While their equations have no closed form, they claim that at small particle sizes the increase in critical resolved shear stress required to move a dislocation can be approximated by:

$$\Delta\tau \approx 0.9 (rf)^{1/2} b \frac{|G_P - G_M|^{3/2}}{G_M^{1/2}} \left[2b \ln \left(\frac{2r}{f^{1/2}b} \right) \right]^{-3/2}$$

where G_P is the precipitate shear modulus, G_M is the matrix shear modulus (10.8 GPa was used as an approximation for pure NiTi), r is the precipitate radius, f is the precipitate volume fraction, and b is the Burger's vector magnitude of the matrix.

From the above equation, it is apparent that increasing the shear modulus of the precipitate will result in a significant strengthening effect (3/2 power dependence). The 1/2 power dependence of r is also approximated as linear similarly to 13.

Since the term $\ln(2r/f^{1/2}b)$ is relatively constant compared to $(rf)^{1/2}$, the above equation for modulus strengthening can be reduced to [23]:

$$\Delta\sigma = K_1 f^{1/2} r$$

where

$$K_1 = 0.9b \frac{|G_P - G_M|^{3/2}}{G_M^{1/2}} \left[2b \ln \left(\frac{2r}{f^{1/2}b} \right) \right]^{-3/2}$$

4.6.2 Other Strengthening Contributions

The contribution of coherency strengthening is given by [38]:

$$\Delta\tau = \alpha_\epsilon G_M \epsilon_{Misfit}^{3/2} \left(\frac{fr}{b} \right)^{1/2}$$

where ϵ_{misfit} is the misfit strain between the precipitate and the matrix, α_ϵ is a coefficient around 3.7, G_M is the matrix shear modulus, r is the precipitate radius, f is the precipitate volume fraction, and b is the Burger's vector magnitude of the matrix [40]. Jung conducted an analysis of the expected strengthening contribution from coherency strengthening and reported an insignificant contribution due to small lattice misfit [34].

As a dislocation shears through an ordered coherent precipitate, an antiphase boundary (APB) is created on the slip plane of the precipitate. The newly formed APB has an associated energy that opposes dislocation motion through the precipitate. However, this defect also attracts dislocations since the passage of another dislocation through the precipitate would eliminate the additional APB energy. This phenomenon is termed

dislocation pair-coupling and can be either strong or weak depending on the tendency for dislocations to repel each other (elastic strain energy).

Huther and Reppich considered the case of strong dislocation pair-coupling, where multiple dislocations may interact with the same particle, while Brown and Ham considered the case of weak pair-coupling, where dislocations lie in different particles [41][42]. Using these models, unrealistically large APB energies ($>400 \text{ mJ/m}^2$) were required to explain the measured strength. As a result, Jung concluded that order strengthening provides an insignificant contribution to the overall strength of the material [34].

The contributions of coherency and order strengthening are thus assumed to be negligible in our design.

4.7 Orowan Looping

At larger precipitate radii and spacing, dislocations will loop around the precipitates. This Orowan looping mechanism is insensitive to the nature of the precipitate itself and is a function of precipitate size, precipitate spacing, and matrix shear properties and can be assumed to be independent of precipitate composition.

The strengthening contribution of Orowan looping is represented by [23]:

$$\Delta\sigma = Kf \frac{1}{L-2r} \frac{Gb}{2\pi\sqrt{1-\nu}} \ln\left(\frac{2r}{r_o}\right)$$

where K is a strengthening coefficient, L is the distance between precipitates, r is the average precipitate radius, G is the matrix shear modulus, r_o is the dislocation core radius, ν is the matrix Poisson's ratio, and b is the magnitude of the matrix Burger's vector.

In addition, L can be approximated as:

$$L = r \left(\frac{2}{f}\right)^{1/2}$$

Combining the two equations above results in the following equation:

$$\Delta\sigma = K_2 \frac{f^{1/2}}{r}$$

from Jiang's thesis K_2 was found to be 3972 MPa/nm [37].

4.7.1 Incipient Melting

A concern associated with the addition of Zr and Al to the NiTi-based SMA is the formation of low-melting phases. Of these, the most problematic phase is the NiTiZr C14 phase, also known as the Laves or λ phase [36]. A study by Hsieh involved researching ternary SMAs with varying Zr content. His research indicated that the λ phase undergoes a solid-liquid phase transition at roughly 930° C [43]. This suggests that the λ phase can promote low eutectic temperatures and that this could cause incipient melting during solutionizing. The λ phase is a concern due to its brittleness and its effect on the final microstructure. It is particularly prone to oxygen pick-up in the liquid phase, which could increase the concentration of oxide inclusions in the final alloy [23]. Another concern is that the addition of Al can affect this phase transition temperature. Bender addressed this in his thesis using a preliminary thermodynamic database in ThermoCalc to simulate the realistic, non-equilibrium cooling conditions to observe the lowest temperature at which liquid phases are still observed. The results are shown in Figure 14.

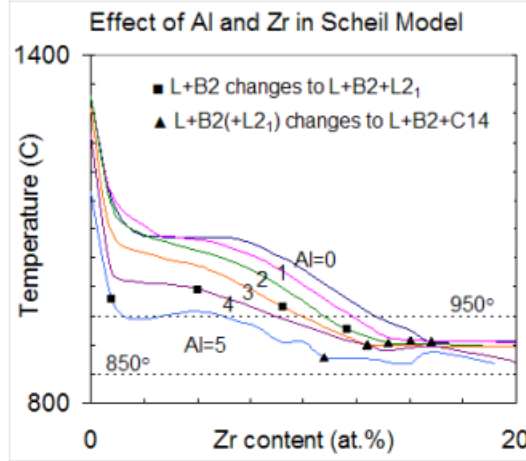


Figure 14: The last remaining liquid as a function of Zr and Al content using the non-equilibrium solidification conditions specified by the Scheil Model [23].

These results suggest that incipient melting can be avoided for alloys with Zr content below 20 at% and Al content below 5 at% as long as all post-processing heat treatments take place below 850 ° C [23]. This was a very important consideration in the final design of the alloy.

4.8 DFT Simulations for Precipitate Strengthening

4.8.1 Background to DFT Simulations

Atomic simulations can be used to illuminate the interactions happening inside the crystal lattice without the complications of actual systems. The method of choice to simulate atomic interactions is Density Functional Theory (DFT). A crystal lattice is filled with numerous electrons which could all be described by their individual wave equations. However, as the Schrodinger Equation evolves into a many bodied problem, it becomes impossible to solve for each electron. Density functional theory is an attempt to treat the problem as a density of electrons, which can be particularly useful in deriving material properties such as molecular or crystal structure, atomic bond lengths, dipole moments, or elastic properties. DFT has a precedent of being used in shape memory alloy systems, such as to determine the effect of hydrogen absorption on crystal structure [44]. For this project, DFT will be used to calculate the bulk modulus of the precipitate Heusler compounds that form with the addition of Zr and Pd alloying additions to the matrix: Ni_2TiAl , Pd_2TiAl , and Ni_2ZrAl . As per literature precedent, the simulation was used to calculate the shear modulus and lattice parameter of the desired compounds and compared to experimental values [45]. The shear modulus was then input into the previously mentioned models to determine the precipitation strengthening in the material.

4.9 Aging Treatment

In order to effectively strengthen the $(\text{Ni,Pd})_{50}(\text{Ti,Zr,Al})_{50}$ alloy and thus increase fatigue lifetime, the optimal precipitate size for efficient strengthening was determined. After this radius was obtained from the strength model in Figure 13, a proper aging treatment was designed. The aging temperature was set to 600°C based on results from previous experimental data.

The proposed strengthening of the hybrid alloy involves precipitating the Heusler $(\text{Ni,Pd})_2(\text{Ti,Zr})\text{Al}$ phase, such that a nanodispersion of these precipitates is formed [18]. The Lee coarsening model was used to predict a proper aging time based on the composition of the alloy, the diffusivities of each element and the predetermined aging temperature.

Ni and Ti Diffusion in B2 NiTi Using radiotracer techniques, the diffusivity of nickel and titanium were experimentally determined in near stoichiometric NiTi alloys in the B2 phase [46]. This method is possible because the appropriate isotopes, ^{63}Ni and ^{44}Ti , exist. The diffusivities of these elements were found to follow linear Arrhenius behavior. A literature search was conducted to obtain experimental values for the pre-exponential factor, D_0 , and activation energy, Q . These values can then be used in the following equation to calculate diffusivity.

$$D = D_0 e^{-Q/RT}$$

Table 3: Experimental values for the pre-exponential factor, D_0 , and activation energy, Q obtained for either Ni or Ti diffusion in the B2 NiTi phase.

Alloy Composition	Element	D_0 (m ² /s)	Q (kJ/mol)	Mechanism	Source
Ni-49.4 at.% Ti	Ni	$(4.7^{+8.0}_{-2.9}) \times 10^{-9}$	142.8 ± 11	Tracer Diffusion	Divinski
Ni-49.4 at.% Ti	Ti	$(2.7^{+2.0}_{-1.2}) \times 10^{-7}$	204.7 ± 6	Tracer Diffusion	Divinski

Al, Zr, and Pd Diffusion in B2 NiTi In order to accurately calculate the aging time required to achieve nanodisperse precipitates of the optimal size, the diffusivities of Al, Zr, Pd, Ni, and Ti in B2 NiTi must be known. However, no diffusion or mobility data was found for Al, Zr, or Pd in ordered B2 NiTi, and therefore our model will involve several assumptions.

There is existing data for Ni and Ti in both the ordered B2 NiTi phase as well as disordered BCC Ti-Ni at 550°C and 600°C. Using the relationships between these two phases, the diffusivity of Al, Zr and Pd can be predicted in B2 NiTi. First, the data points for Ni and Ti in both phases at 550°C and 600°C were plotted in Figure 15. Because Zr and Al atoms sit on the Ti sublattice, the linear trend for Ti can be used to predict the diffusivity of Zr and Al in B2 NiTi based on their diffusivity in BCC NiTi. The diffusivities for Zr and Al in the BCC phase were found using the relevant DICTRA databases. The same can be done for Pd, which sits on the Ni sublattice. However, because there was no mobility database in DICTRA for Pd in BCC NiTi, the diffusivity was obtained for Pd in BCC Ti. From this value, Pd diffusivity in B2 NiTi was predicted. Table 4 gives the diffusivity values for all of the elements in the alloy in both the disordered BCC NiTi or BCC Ti as well as the literature and predicted diffusivities in ordered B2 NiTi.

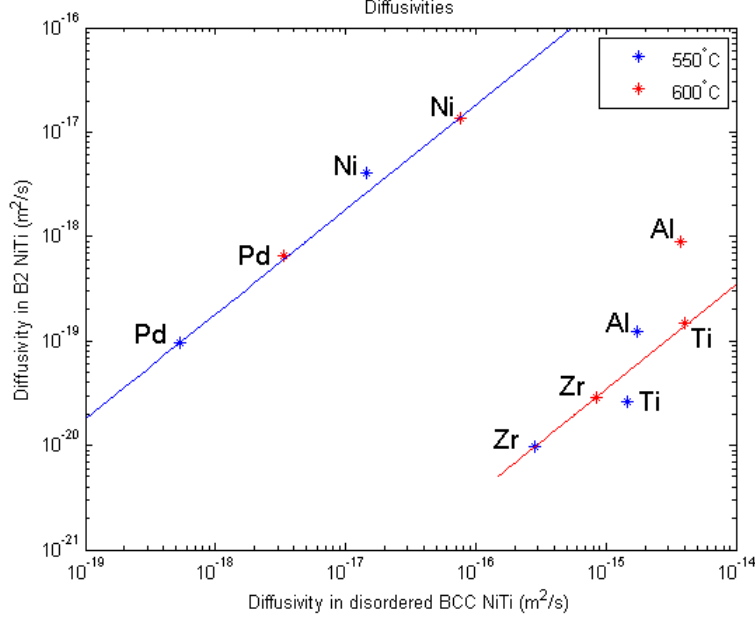


Figure 15: Diffusivities of Ni, Ti, Zr, Al and Pd in the ordered B2 NiTi phase and the disordered BCC NiTi phase at 550 ° C and 600 ° C.

Table 4: Diffusivity values for the alloying elements in disordered BCC NiTi or BCC Ti, as well as literature and predicted diffusivities of the respective elements in ordered B2 NiTi.

	D in disordered BCC NiTi	D in ordered B2 NiTi
Ti	4.054 E-15	1.469 E-19
Pd	3.347 E-18 (in BCC Ti)	6.014 E-19
Zr	8.507 E-16	2.909 E-20
Al	3.736 E-15	1.278 E-19
Ni	7.646 E-17	1.346 E-17

The diffusivities calculated for each element in B2 NiTi can then be used in the Lee coarsening model to predict a proper aging time at 600°C. This model is described by the following equation:

$$\bar{r}^3 - \bar{r}_o^3 = \frac{4}{9} K t$$

In this case, r_o was taken to be zero and the optimal precipitate radius at time t was determined previously in Figure 13. Next, the following equation for the coarsening constant, K :

$$K = \frac{2\sigma V_m^\beta}{RT} \left[\sum_M (k_M - k_1) (k_M - 1) \frac{x_M^\beta}{D_M^\alpha} \right]^{-1}$$

where $k = x_i^\alpha/x_i^\beta$; α is the B2 phase, β is the L21 phase, and Ti is taken to be component 1. V_m^β is the molar volume of the Heusler phase and was previously calculated in the misfit model. Lastly, the interfacial energy term, σ , for a given composition was calculated according to the equation:

$$\sigma = (-11.11mJ/m^2 * X_{Pd}^{L21} - 229.73mJ/m^2 * X_{Zr}^{L21} + 201mJ/m^2)/1000$$

where X_{Pd}^{L21} is the site fraction of Pd in L21 and ranges from 0 to 2, and X_{Zr}^{L21} is the site fraction of Zr in L21 and ranges from 0 to 1.

4.9.1 Misfit

It is important to minimize the misfit that arises from differences in lattice parameters so that during transformation, there is no irreversible loss of coherency at the L2₁-B2 interface. An interface with high interfacial energy, such as an incoherent interface, will increase the rate of coarsening. Therefore, misfit should be minimized to maintain coherency and maximize the driving force for particle refinement [47]. The goal for this alloy design was to keep misfit under 1%, comparable to the 1.07% and 0.71% misfit values used in comparable systems for Jung’s thesis and Bender’s thesis respectively [34, 23]. In contrast, if there is a loss of coherency at the interface, dislocations will be created, as can be seen in Figure 16. The misfit between the B2 matrix phase and L2₁ Heusler phase was calculated using following equations, where δ is the misfit, $\bar{\Omega}$ is the average atomic volume, and x is the mole fraction of each alloying element.

$$\delta = \sqrt[3]{\frac{\bar{\Omega}_{L2_1}}{\bar{\Omega}_{B2}}} - 1$$

$$\bar{\Omega}_{L2_1} = \sum_{i=1}^n x_i \times \bar{\Omega}_i^{L2_1}$$

$$\bar{\Omega}_{B2} = \sum_{j=1}^n x_j \times \bar{\Omega}_j^{B2}$$

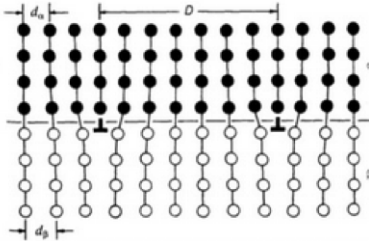


Figure 16: A semi-coherent interface, which results in misfit dislocations that reduce the elastic energy of the system at the expense of an increase in interfacial energy [47].

4.9.2 Modeling Software

ThermoCalc is a software that performs thermodynamic calculations, allowing users to calculate thermodynamic equilibria in materials. Using a thermodynamic database created by Dr. Wei-Wei Zhang, the aging temperature, 600°C, and bulk composition was input to obtain the solution temperature, phase compositions, and phase fractions of the system. The database includes thermodynamic data for palladium, which had not been included in previous databases. ThermoCalc was used to ensure that the resulting composition has the desired B2 matrix phase and L2₁ Heusler precipitate phase. In addition, ThermoCalc was used to verify that our design does not result in the presence of additional unwanted phases and/or incipient melting. Because ThermoCalc performs calculations at thermodynamic equilibrium, a capillary energy term and an energy correction term were incorporated to allow for the calculation of non-equilibrium aging conditions. The capillary energy term accounts for the curvature of the nanoprecipitates and the energy correction accounts for the addition of Pd.

DICTRA (Diffusion Controlled Transformation) is a computational tool that performs mobility and thermodynamic calculations. DICTRA was utilized to aid in the design of a nanodispersion strengthened alloy with Heusler phase precipitates of the optimal size. Various mobility databases were utilized to calculate the diffusivity of Al, Pd, Zr, Ni and Ti in the BCC NiTi or BCC Ti phases. These diffusivities were then used in the Lee coarsening model to predict an aging time at 600°C.

4.10 Transformation Temperature

A Redlich-Kister polynomial model will be used to model the transformation temperature as a function of composition. The general form of the Redlich-Kister model is:

$$A_f = \sum_{i=1}^p y_{A_i}^I \sum_{j=1}^q y_{B_j}^{II} \cdot A_{f(A_i:B_j)}^0 + \sum_{i=1}^p \sum_{j_1=1}^q \sum_{j_2=1}^q y_{A_i}^I y_{B_{j_1}}^{II} y_{B_{j_2}}^{II} \cdot L_{(A_i:B_{j_1},B_{j_2})}^k \cdot (y_{B_{j_1}}^{II} - y_{B_{j_2}}^{II})^k + \sum_{j=1}^q \sum_{i_1=1}^p \sum_{i_2=1}^p y_{B_j}^{II} y_{A_{i_1}}^I y_{A_{i_2}}^I \cdot L_{(A_{i_1},A_{i_2}:B_j)}^k \cdot (y_{A_{i_1}}^I - y_{A_{i_2}}^I)^k$$

where $A_f^0(A_i:B_j)$ are interaction parameters for each element in the alloy. Relative amounts of each element were manipulated so that the desired A_f of 10°C-15 °C is achieved. Interaction parameters can be calculated from existing data and a new interaction parameter will be calculated for the Al-Zr system based on experimental data [48].

Table 5: Table of Interaction Parameters for the Redlich-Kister Polynomial

Sublattice I	Sublattice II			
		Ti	Al	Zr
	Pd	591	-2272.32	245.36
Ni	89	-7245	1217.3	

Table 6: The higher-order L_0 and L_1 terms used in the contour plots of the Redlich-Kister equation.

	L_0	L_1
(Ni,Pd):Ti	-720.43	-507.46
Ni:(Zr,Ti)	-919.32	-

4.11 Radiopacity

The transmission of X-rays through a material is determined by its mass attenuation coefficient. The mass attenuation coefficient for an alloy can be found with a weighted sum of each element's respective mass attenuation coefficient:

$$\left(\frac{\mu}{\rho}\right) = \sum w_i \left(\frac{\mu}{\rho}\right)_i = k\lambda^3 Z_{eff}^3$$

where k is a constant, λ is the wavelength of the incident light, and Z_{eff} is the effective atomic number of the alloy. Z_{eff} can be found using the following equation:

$$Z_{eff} = \sqrt[2.94]{\sum f_i \times Z_i^{2.94}}$$

Here f_i is the fraction of total atoms associated with each element in the alloy and Z_i is the atomic number of each element. From this model it is evident that elements with higher atomic numbers will make the alloy more radiopaque. The design approaches focused on adding elements with higher atomic numbers to increase radiopacity.

Mass attenuation coefficients for each element were found from the NIST database over a range of photon energies [28]. A photon energy of 30 keV was chosen because this is a typical value for medical X-rays [49]. The mass attenuation coefficient of the alloy was found by finding the mass fraction of each element from the bulk composition and taking a weighted sum of the individual mass attenuation coefficients at 30 keV.

5 Powder Metallurgy

The final properties of NiTi-based SMAs are very sensitive to the processing methods used during fabrication. The traditional VIM/VAR technique is very expensive due to the high temperature required for melting (above 1300 °C) and the subsequent treatments required for strengthening and forming the final product. These processes include hot working, cold working, heat-treating for precipitate formation, machining, joining, and finishing [50].

Research into more economical methods has shown that powder metallurgy presents a viable alternative. It has the potential to form near-net shape components, which would significantly cut down the stages needed in forming parts. Conventional methods present issues with density and homogeneity, but several research papers provide solutions that could result in methods that produce acceptable alloys.

5.1 Mechanical Alloying

Powder metallurgy can be performed using elemental powders or pre-alloyed powders. Research has suggested that the use of pre-alloyed powders can improve the homogeneity of the end product, suppress the formation of intermetallic phases, and allow precise control of the transformation temperature [51, 14].

Mechanical alloying is a multi-step process that involves fragmentation, deformation, cold welding, and short-range diffusion of elemental powders within a high power ball mill [52]. There are four main ball mills that can be used for this purpose: a vertical ball mill such as an attritor mill, a vibratory mill such as the SPEX shaker mill, a horizontal mill, or a planetary ball mill. In a study by Sadrnezhad and Selahi, mechanically alloyed NiTi was analyzed to observe the effects of milling time and milling speed on both the alloyed powder and the final structure of samples after sintering and annealing. In general, the porosity of the sintered sample decreased with longer milling times. This is because pre-alloying the powders reduces Kirkendall porosity in the final sample due to the faster diffusion of Ni in Ti. It also eliminates the porosity that can occur when Ni and Ti combust to form NiTi during sintering of elemental powders. The presence of intermetallic phases, namely Ni₃Ti, peaked at 4% around 12 hours of milling and then decreased with further milling time [52]. This occurred due to the difference in diffusion coefficients of Ni and Ti, as well as the particle size. Longer milling times allowed more diffusion to occur, which promoted the formation of particles with compositions closer to the equiatomic ratio. It has also been shown that mechanically alloying Ni, Ti and Zr can suppress the formation of the Laves phase, which can create incipient melting and embrittlement of the material [51].

The transition temperature was affected by the refinement of the powder particles and the stored energy within the particles due to deformation. The stored energy promotes recovery, recrystallization, and growth during sintering and annealing, which create larger grains. Grain boundaries serve as nucleation sites for martensite plates, so decreasing the overall grain boundary area by increasing grain size will make it more difficult for the B2-B19' transformation to occur [53]. Thus, larger grains effectively reduce the transformation temperature. The final composition of the powder particles depended on the extent of diffusion that occurred. Faster milling speeds promoted faster diffusion, and, as previously mentioned, longer milling times led to more equiatomic powder particles [52].

In general, mechanically alloyed powders reduce many of the inhomogeneities and porosity observed in alloys made from pure elemental powders. However, it should be mentioned that the oxygen content is likely to increase during milling. The best results occur when milling occurs in an inert atmosphere, such as an argon atmosphere [52]. Unfortunately, even the smallest amount of oxygen in the atmosphere will cause oxidation due to the high surface area of the powder and the high reactivity of Ti with O. The oxygen content of all affordable powders poses a problem, but the properties afforded by mechanically alloying powders shows potential for the use of powder metallurgy in the production of shape memory alloys.

5.2 Sintering Methods

An important stage in creating a final product using powder metallurgy is sintering. In this stage, pressure and/or heat is applied to the powder to form a shape. Diffusion occurs during this time to bind the powder particles together. As previously mentioned, porosity and homogeneity have been a problem with conventional hot-press sintering methods [54]. The problems with homogeneity can be partially solved by using mechanically alloyed powders. However, the sintering environment is very important to ensure that impurity introduction is minimized at this stage. One suggestion is to use vapor phase calciothermic reduction (VPCR) during sintering. This process uses a reducing atmosphere made up of calcium vapor in order to deoxidize the powder and increase the purity of the alloy [55]. Oxidation typically occurs on the surface of powder particles, especially with Zr and Ti, so deoxidizing can also enhance the solid-state diffusion that occurs during sintering [55]. Enhancing the diffusion will help to decrease the porosity of the final material by creating more direct interfaces between the powder particles.

The porosity of final products can also be reduced by using spark plasma sintering (SPS). In this process, a uniaxial pressure is applied to powder loaded into a graphite die. Then, heat is applied by sending electric pulses through the material. The electric pulses heat each powder particle individually, which is much more efficient than traditional hot-pressing. The entire sintering process can occur very quickly, and lower temperatures can be used because of this efficiency. The efficiency of heating and applied pressure in SPS can produce alloys with greater than 99% theoretical density [54]. It should also be noted that a graphite die is used in this process, which could lead to carbon diffusion and subsequent carbide impurities much like the graphite crucibles using in VIM. However, SPS is carried out at much lower temperatures because this is a solid-state process, so carbon diffusion will likely be reduced.

5.3 Gettering of Oxygen

Inexpensive titanium powder poses a problem due to its high oxygen content. This occurs because of the high surface area-to-volume ratio of powder, so oxygen is more readily dissolved. Oxygen stabilizes some intermetallic phases in the Ni-Ti-Zr system, which can strongly affect the Ni-Ti ratio within the matrix. The shape memory effect is very sensitive to this ratio, for it only occurs for near-equiatomic proportions (B2 phase). Straying from this composition can also have a large effect on the transformation temperature. Even differences in a fraction of an atomic percent can affect this temperature, which is a very important design parameter. Though VCPR sintering shows promise in reducing oxygen content, oxygen gettering has been proven effective to scavenge oxygen from the matrix. In order to create alloys with acceptable ductility and Ni-Ti ratios in the matrix, elements must be introduced in small amounts to getter oxygen from the matrix. The acute reactivity of rare earth metals makes them very effective getters. Since the 1990s, rare earths have been used in PM to improve the properties of Ti alloy [56]. Of the rare earths, yttrium has the highest affinity for oxygen and is near Ti on the periodic table, making it the best choice as an oxygen getter in Ti alloys [57]. In general, the most effective way to introduce yttrium in powder form is by creating a powder of its hydride, YH_2 [56, 58]. This is because the introduction of Y already in its oxide form has very little gettering ability, and keeping a powder of pure Y is virtually impossible due to its high reactivity. YH_2 is unstable at elevated temperatures, which causes its decomposition and leaves pure Y in the alloy [56, 58].

The mechanism by which oxygen gettering occurs during sintering of PM Ti alloys has been studied by in situ synchrotron radiation. Yan, et al studied the behavior of YH_2 in both commercially pure Ti and Ti-6Al-4V. The results of this study showed that the stability of YH_2 changes depending on the elements present; in the pure Ti, YH_2 decomposed above 900 ° C while it decomposed above 1100 ° C in Ti-6Al-4V [58]. This is of interest for this alloy design because the compositions could affect the temperature stability of YH_2 . The results of this experiment suggest that the initial formation of Y_2O_3 precipitates depends on the diffusivity of oxygen through the matrix, but the subsequent scavenging rate is limited by the diffusivity of oxygen through the Y_2O_3 surface layer on Y particles, as shown in Figure 17.

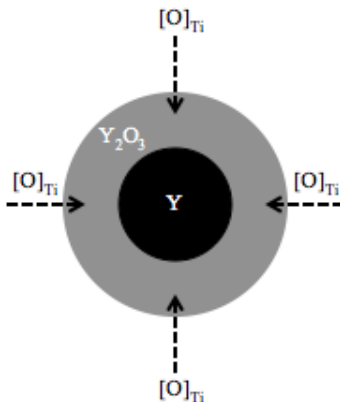


Figure 17: Schematic of the yttrium oxide formation by diffusion of oxygen from the matrix through the Y_2O_3 surface layer [58].

These Y_2O_3 particles are still oxides that can have sizes on the μm -scale, which could still have adverse effects on the fatigue properties of the SMA. Fatigue tests of a Ti-Nb-Ta-Zr alloy (TNTZ) with various levels of Y_2O_3 additions showed that fatigue properties improve when the Y_2O_3 particle size is below 1 μm , but that they serve as crack initiation sites when greater than this size [59]. A typical NiTi sample manufactured by VIM has oxygen content of about 220 ppm by weight, or 0.022 mol% [48]. In order to get all of the oxygen, about 0.015 mol% Y should be added using stoichiometric considerations. In research with Y_2O_3 in TNTZ showed that additions of 0.05 wt% Y, or 0.03 mol%, created precipitates on the order of 100 nm [59]. The precipitates formed from adding 0.15mol% Y will remain on the nanometer scale, so their potency as fatigue crack nucleation sites will be acceptable. It is likely that the new alloy designs will have a higher oxygen content, especially if powder metallurgy is used as the processing method. Song et al found that the precipitates will remain on the nanometer scale as long as less than 0.2 wt% of Y is added, The size of the oxides can also be reduced by ensuring a homogeneous distribution of Y before sintering so that Y particles are less likely to coalesce [54]. Adequate mixing of Ni, Ti, and Zr was reported after milling for 0.6 ks in a planetary ball mill, which is too short for alloying to occur [51]. A similar process could be used to produce a more homogeneous distribution of YH_2 .

Yttrium gettering is a promising method to improve the properties of NiTi-based SMA's. In order to determine the proper time and temperature needed to fully getter oxygen from the matrix, both the diffusivity of solid solution oxygen within the matrix and through Y_2O_3 must be determined. The formation of these oxides will inhibit the formation of Ti_4Ni_2O , which will ensure that the matrix has the correct ratio of Ni and Ti. In order to minimize the adverse effects of Y_2O_3 particles, the size of the oxide particles should be as small as possible. Limiting the mass percent of Y added to the alloy and evenly distributing the YH_2 powder before sintering can achieve this. However, further research must be conducted in order to accurately predict how these new oxides will behave in the new alloy.

6 Results

6.1 DFT Calculations

6.1.1 DFT Calculation Approach

The DFT calculations were done using the Quantum Espresso software package, a program that the Northwestern QUEST supercomputer cluster can run.

Experimental Model of the System Initially, a supercell of the crystal structure of the Heusler phase must be created based on experimental values for the lattice parameter of different compositions. This model was created using the software VESTA, which is able to design crystal unit cells and export atom locations. This is a critical input for the DFT calculations, as the initial crystal gives the Quantum Espresso algorithm a starting point to calculate a relaxed crystal system. The properties of the calculated crystal will differ from the experimental data because DFT assumes a system at 0K to avoid complicating factors like phonon vibrations, along with simplifying the potential acting on the electrons to lower processing time.

Creating a Mesh After the initial crystal is entered, an appropriate set of approximations, the energy cutoff and the k-point grid, needs to be determined to model the system accurately. In order to determine these parameters, increasing values of the energy cutoff and k-point grid (and therefore a finer mesh) are entered in the model with the experimental lattice parameter, and the energy of the system is recorded. As the mesh shrinks, the energy of the system converges on a single value, and at that point of convergence the mesh is at an appropriate size. To find the convergence point, a series of data points needs to be collected, which is done by writing a Bash script to iteratively request the Quest supercomputer to perform an energy calculation with the differing parameters. Bash is a language used to interface with Linux computers and can be used to repetitively run different commands.

Self Consistent Field Method To calculate the energy, Quantum Espresso uses the self-consistent field method (SCF). In this method, an initial energy is assumed, and then used to derive a Hartree equation which functions as an approximate solution to the Schrodinger Equation. This can then be used to calculate an energy of the system, which is compared to the initial input energy. When these values are found to be self consistent, the calculation terminates. After this calculation is run several times to find an appropriate mesh size, a relaxed lattice parameter can be calculated. This is found in a similar manner, with a Bash script to loop through several possible lattice parameters, and the energy calculated at each size. Changing the lattice parameter will have a parabolic effect on the energy of the system, with the minimum of the curve occurring at the equilibrium lattice parameter. It is important to note that Quantum-Espresso uses the units of Bohr (1 Bohr = .5292 Angstrom) for distance and Rydberg (1 Ry = 13.6057 eV) for energy [60].

Calculating Elastic Properties The energy-lattice parameter curve was recalculated to be an energy-volume curve. The curvature of this function is equal to the bulk modulus.

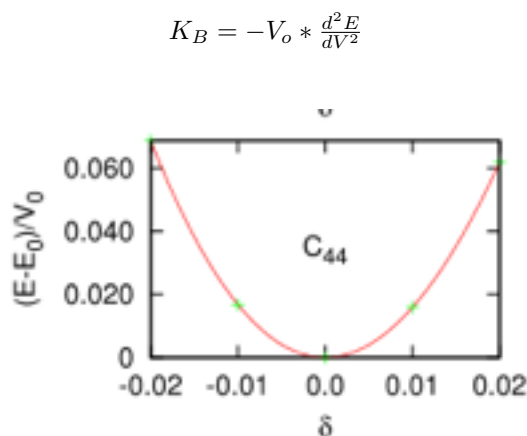
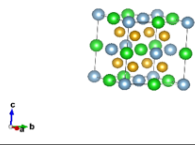
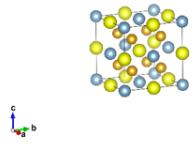
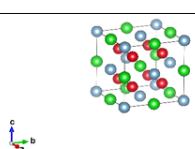


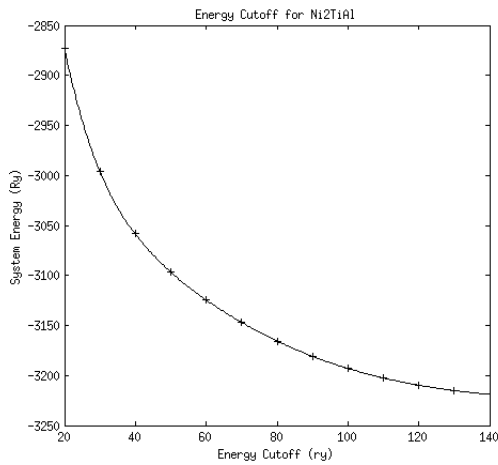
Figure 18: Energy deformation curve of an example Ni₂MnGa crystal used to find its shear modulus [61].

Results are shown in Table 7:

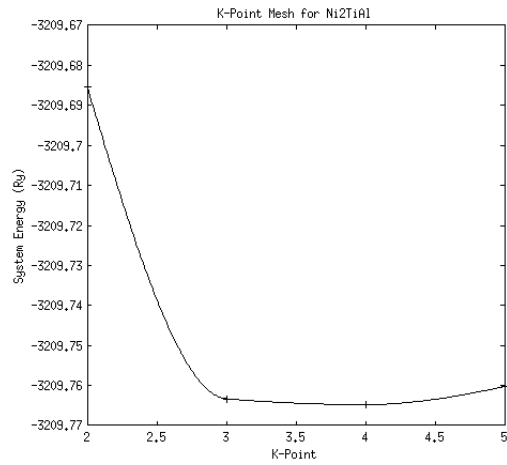
Table 7: Preliminary results for DFT simulations of various precipitate structures

	Crystal Structure	Experimental Lattice Parameter (Å)	Calculated Lattice Parameter (Å)	% Difference
Ni ₂ TiAl [62]		5.88020	5.9321	0.88%
Ni ₂ ZrAl [63]		6.03216	6.075	0.71%
Pd ₂ TiAl [64]		6.32200	6.3501	0.44%

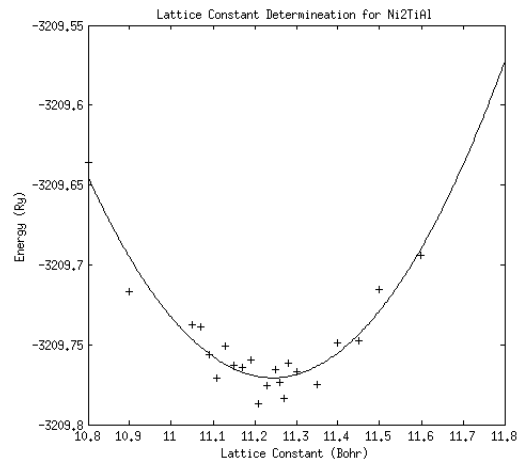
The following figures show the calculated convergence curves. The curvature was determined by taking the derivative of the fit to the lattice vs energy curve:



(a)



(b)



(c)

Figure 19: (a) Plot of finding the energy cutoff convergence for the Ni₂TiAl crystal. This data approaches a convergence at 120 Ry. (b) K-Point mesh for the Ni₂TiAl crystal. This reaches a convergence with a mesh of either 3 or 4. A value of 4 is used to ensure accuracy. (c) Effect of changing the lattice constant on the energy of the system. The minimum of this function is the equilibrium lattice constant, which is determined to be 5.9321 Å. Moreover, this function's curvature can be used to calculate the bulk modulus.

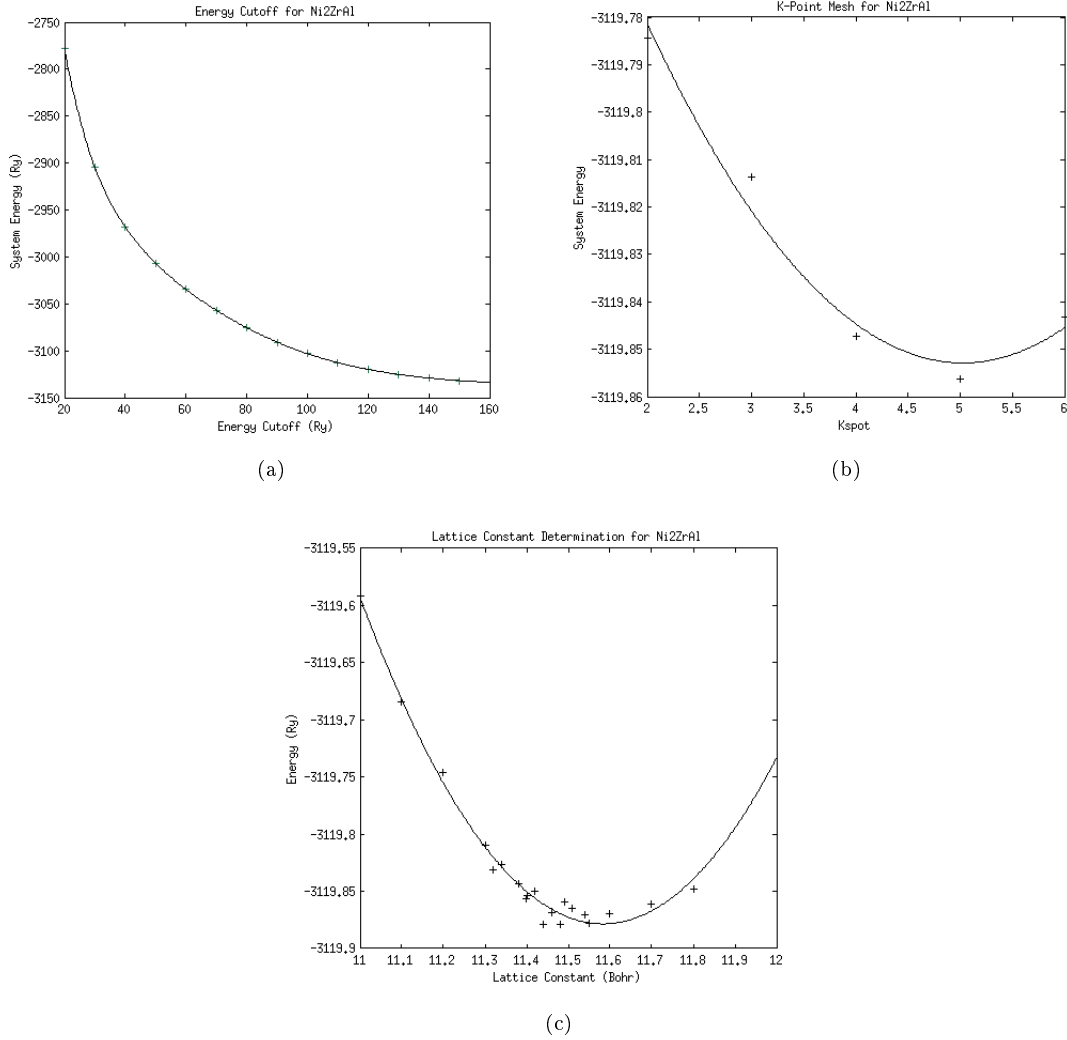


Figure 20: (a) Plot of finding the energy cutoff convergence for the Ni_2ZrAl crystal. This data reaches a convergence at 120 Ry. (b) K-Point mesh for the Ni_2ZrAl crystal. This already seems fairly converged at a mesh of 2, but becomes even more precise with a mesh of 4. (c) Effect of changing the lattice constant on the energy of the system. The minimum of this function is the equilibrium lattice constant, which is determined to be 6.075 Å. Moreover, this function's curvature can be used to calculate the bulk modulus.

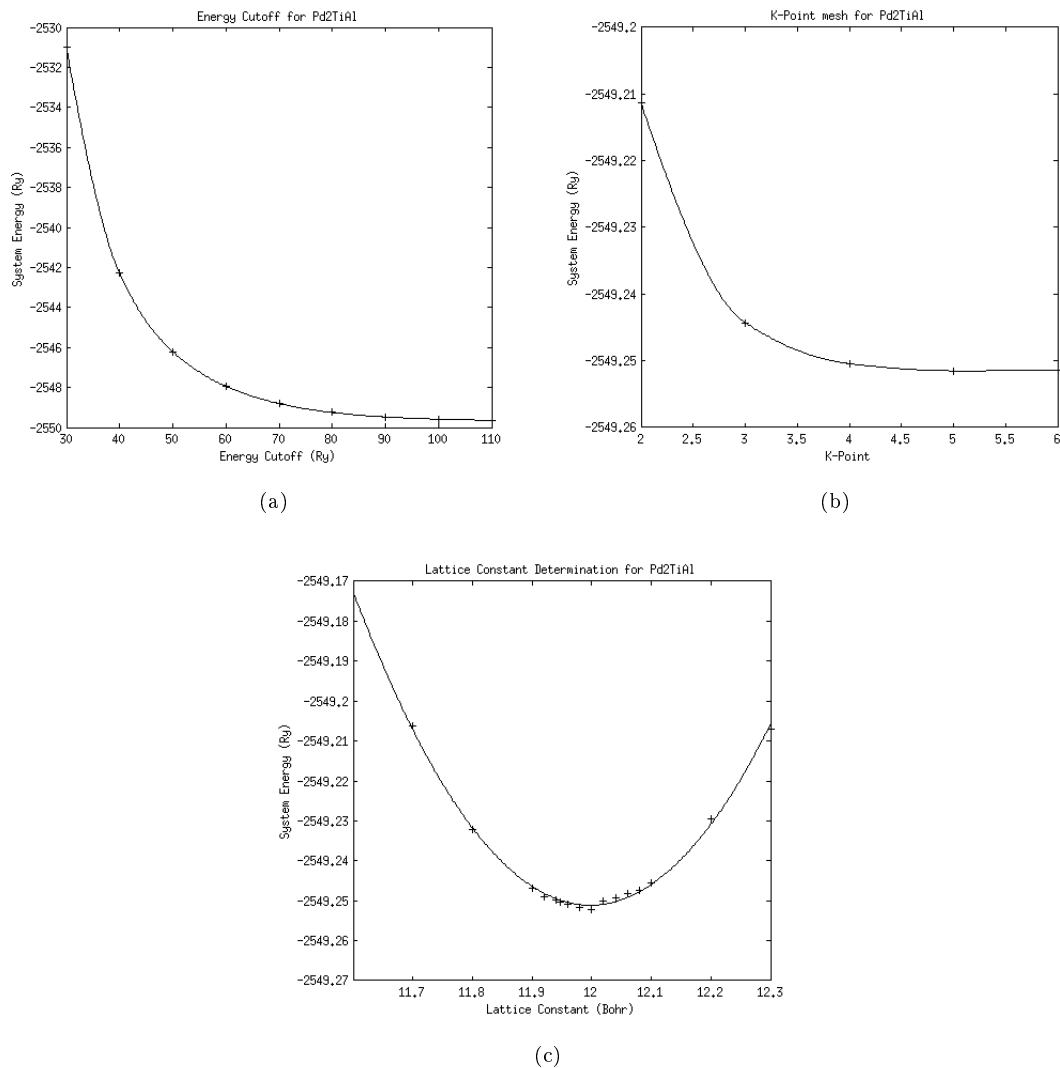


Figure 21: (a) Plot of finding the energy cutoff convergence for the Pd₂TiAl crystal. This data reaches a convergence at 80 Ry. (b) K-Point mesh for the Pd₂TiAl crystal. This reaches a convergence with a mesh of 4. (c) Effect of changing the lattice constant on the energy of the system. The minimum of this function is the equilibrium lattice constant, which is determined to be 6.3501 Å. Moreover, this function's curvature can be used to calculate the bulk modulus.

Table 8: Values of the estimated bulk moduli of each compound and calculated isotropic shear moduli assuming a Poisson's ratio of 0.33.

Compound	Bulk Modulus (GPa)	Shear Modulus (GPa)
Ni ₂ TiAl	188.3	72.2
Ni ₂ ZrAl	251.9	96.6
Pd ₂ TiAl	134.9	51.7

The isotropic shear moduli in Table 8 were found by utilizing the following equation and assuming a Poisson's ratio of 0.33 for the matrix phase.

$$G = \frac{3K(1-2\nu)}{2(1+\nu)}$$

6.2 K1 Model and Capillary Energy Determination

To find appropriate estimates for the intersection of the precipitate shearing and Orowan looping curves, a model was employed to find the K_1 of shearing for varying Pd and Zr concentrations. The steps taken to find K_1 and ultimately the capillary energy for a given Heusler phase composition are as follows:

1. Shear moduli for the three endpoints were plotted against composition to find a plane surface of moduli modeled as a linear combination of Zr and Pd.

(a) $G = -10.24 * Pd + 48.76 * Zr + 72.21$ where Pd varies from 0 to 2 and Zr varies from 0 to 1

2. Using this plane of moduli, the data mentioned earlier from Bender and Jiang was used to predict shear moduli from these experimental points.
3. The known K_1 values for these two alloys (393 MPa/nm from Bender and 1433 MPa/nm from Jiang) were divided by the shear modulus dependence shown in the equation below [23, 37].

$$\Delta\tau \approx 0.9 (rf)^{1/2} b \frac{|G_P - G_M|^{3/2}}{G_M^{1/2}} \left[2b \ln \left(\frac{2r}{f^{1/2}b} \right) \right]^{-3/2}$$

4. This proportionality constant was averaged for the Bender and Jiang points (0.01522) and then used for the three endpoints calculated by DFT.
5. By knowing the K_1 for any composition of Zr and Pd (22), the intersection with the Orowan looping curve and the precipitate shearing curve can be found and the optimum radius for strengthening can be calculated (23.)
6. The optimum radius is used to find the capillary energy addition to be added to non-equilibrium calculations in ThermoCalc. The interfacial energy found in the capillary energy addition was found by fitting experimental data to a plane as a function of composition.
7. Another energy correction was also calculated to be added to these non-equilibrium calculations. This term accounts for the difference between predicted and observed solubilities for Al in the B2 matrix. Experimental data were fit to a plane similar to the method used in the K1 calculation to find this corrective energy term as a function of composition.

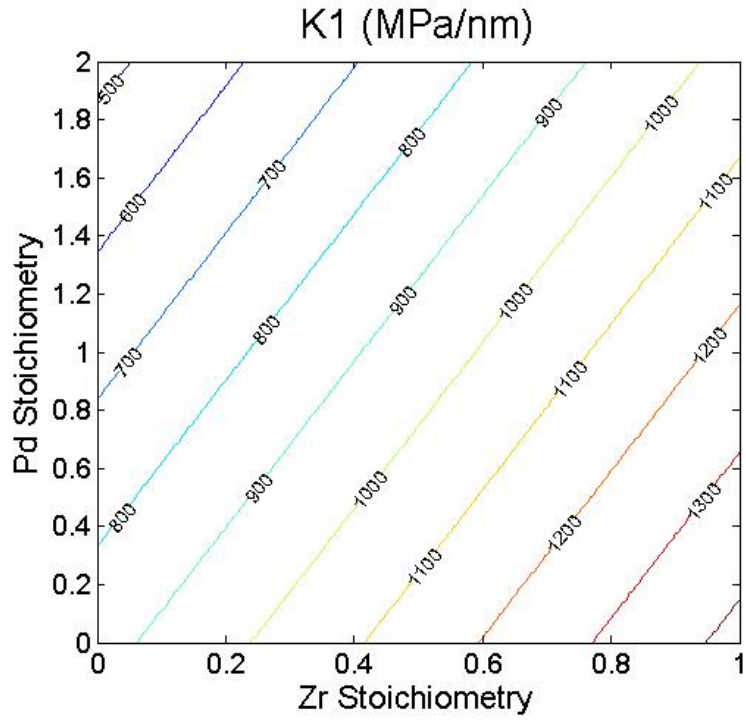


Figure 22: K1 Plane Calculated from DFT and Fit to Experimental Data

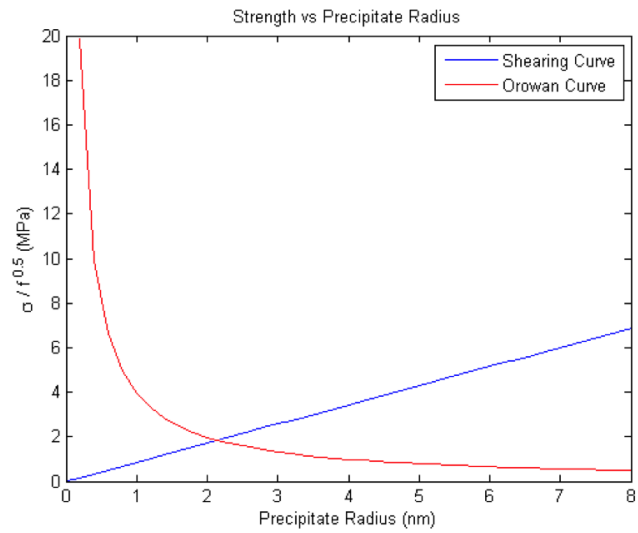


Figure 23: Shearing vs Orowan Looping Curve to Determine Optimum Precipitate Size

6.3 Final Alloy Design

Table 9: Final composition values for the bulk alloy and constituent phases.

Bulk Composition	$\text{Ni}_{29.5}\text{Pd}_{20.5}\text{Ti}_{32.95}\text{Zr}_{13.15}\text{Al}_{3.9}$
B2 Matrix Phase Composition	$\text{Ni}_{31.9}\text{Pd}_{18.1}\text{Ti}_{36.09}\text{Zr}_{12.97}\text{Al}_{0.94}$
L21 Heusler Phase Composition	$\text{Ni}_{12.33}\text{Pd}_{37.67}\text{Ti}_{10.54}\text{Zr}_{14.46}\text{Al}_{25}$

Table 10: Property and Objective Values for Bulk Alloy

Property/Objective	Alloy Value	Target Range
Transformation Temperature ($^{\circ}\text{C}$)	14.1	10-15
Yield Strength (MPa)	2523	>2000
Misfit (%)	0.99	<1
Mass Attenuation Coefficient Improvement (%)	241	–
Phase Fraction (%)	12.28	–
Optimum Precipitate Radius (nm)	2.15	–
Aging Time at 600 $^{\circ}\text{C}$ (hours)	29.2	–
Solution Temperature ($^{\circ}\text{C}$)	690	–
Equilibrium Energy Shift (J/mol)	1874	–

Although all of the design objectives for this alloy design were met, it can be seen in Figure 24 that the misfit for the designed alloy is very near the design objective. There was a very narrow design window in which both the transformation temperature and the misfit both matched the design requirements ($A_f=10-15^{\circ}\text{C}$ and $\text{misfit}<1\%$), denoted by the gray shaded area. The designed composition (red dot in 24) had restrictions of the palladium content to below approximately 21 mol% in the bulk composition due to instabilities in the newly-created Pd-containing thermodynamic database. In the ThermoCalc equilibrium calculations, it was seen that Pd content above 22 mol% resulted in a deficiency of aluminum in the matrix phase. In contrast, previous experimental studies have shown that increasing the palladium in this system should increase the aluminum solubility in the matrix phase. Greater palladium concentrations can be explored as the interaction parameters in the database are updated to more accurately describe the thermodynamics of the alloy.

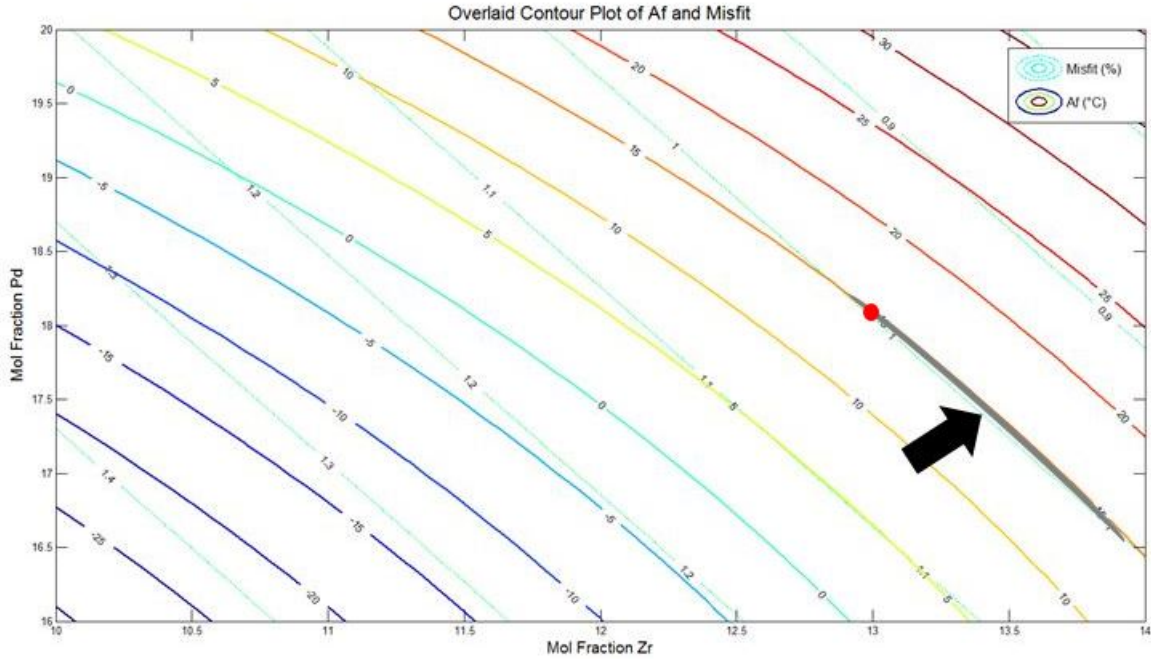


Figure 24: Transformation Temperature and Misfit Crossplot

As the model is updated, it is expected that increasing palladium will begin decreasing the misfit, but will also decrease the Heusler phase fraction which will ultimately decrease the yield strength. This final alloy design is roughly 500 MPa over the yield strength objective so there is design space to move the composition to higher palladium. Both the yield strength and the radiopacity were met over the entire Pd and Zr ranges that were investigated (Figures 25 and 26 respectively.)

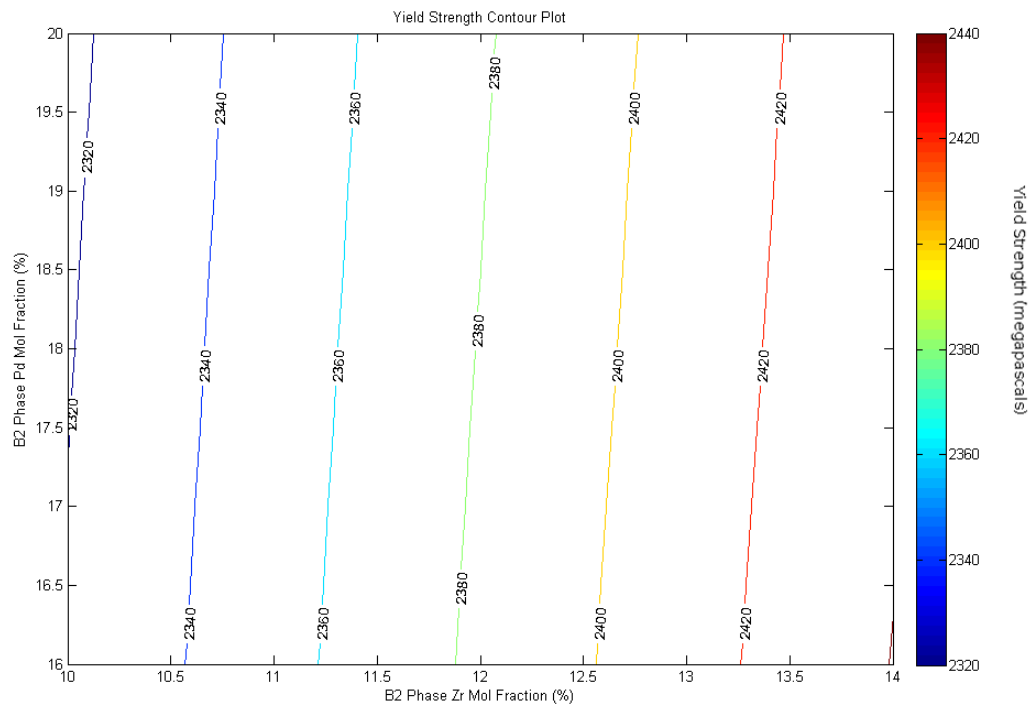


Figure 25: Yield Strength Contour Plot

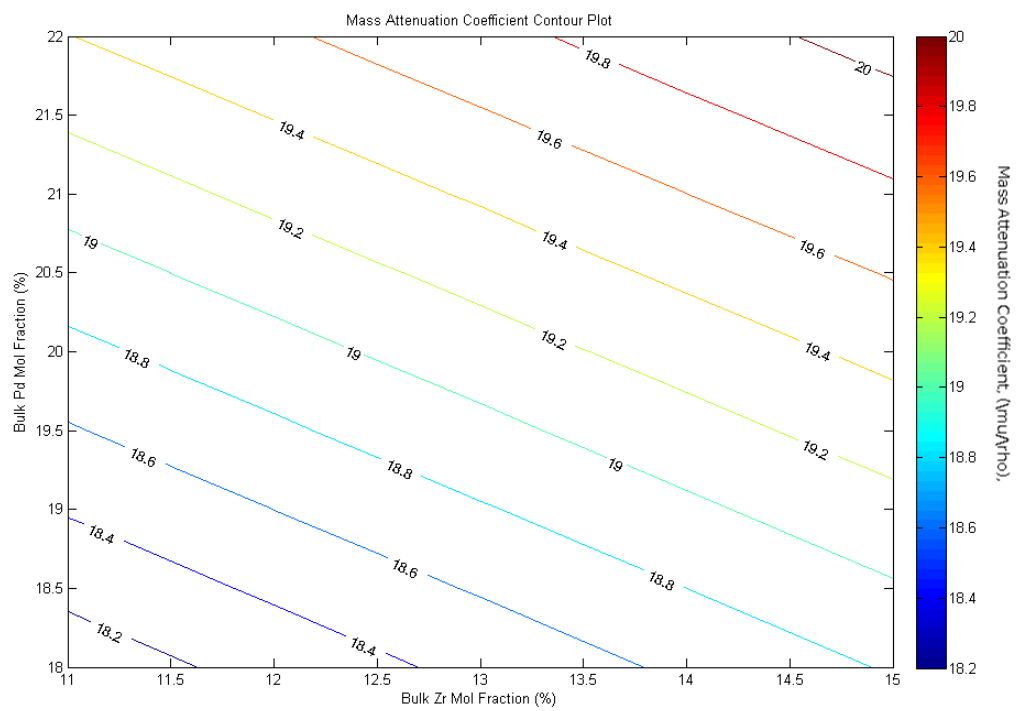


Figure 26: Radiopacity Contour Plot

A map of a palladium free alloy was used to circumvent the thermodynamic instabilities seen in the Pd-containing database. The nickel content was set to 50% and the zirconium content was set to 13.5%. Aluminum content was varied with temperature and the resulting step diagram was adapted for a palladium alloy. This was done by shifting the solvus temperature on the aluminum lean side of the phase diagram by 0.8 mol%, consistent with experimental data. Jiang showed that the Al solubility in a NiTiZrAl alloy is 2.2% whereas Bender showed that the Al solubility in a NiPdTiAl alloy is 3.0%, a change in solubility of 0.8%. This shifts the solution temperature downward for the same aluminum concentration. The solution temperature model is another part of this design process that will become significantly more accurate as the ThermoCalc database is updated. Figure 27 shows that the solution temperature is 690°C, below the expected range of values. Updated thermodynamic modeling with remove estimations like this and a real solution temperature can be calculated.

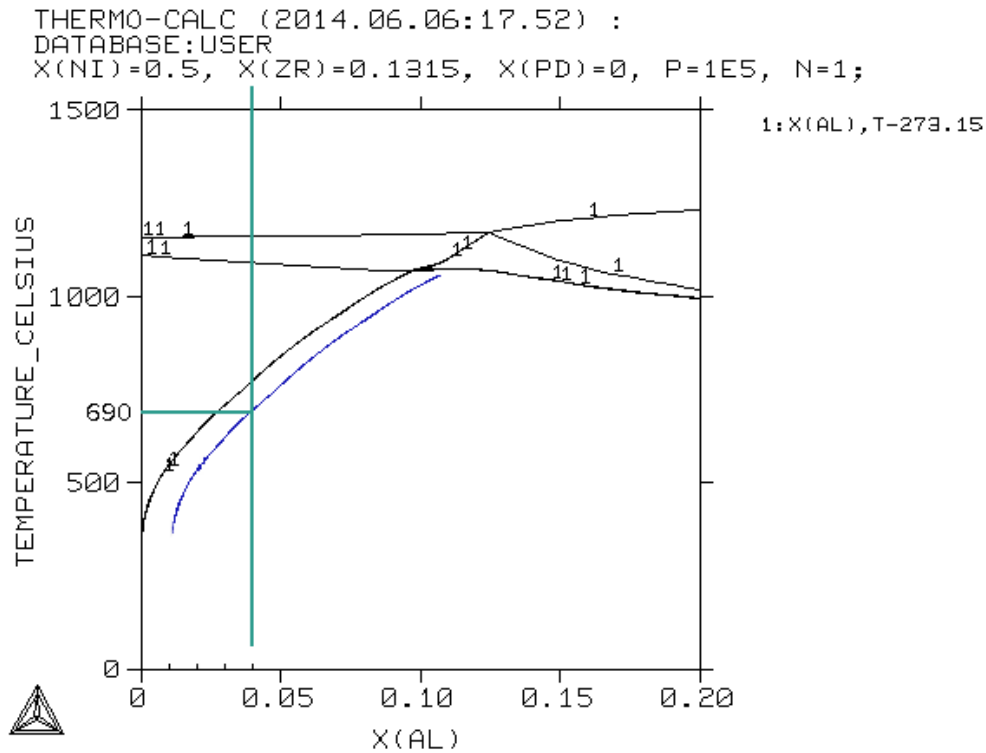


Figure 27: Phase Diagram with Palladium Shift for Solution Temperature Determination

Coarsening rates for this alloy system were higher than expected; likely due to the estimations made in the diffusivity data measurements. This led to aging times that were slightly higher than typical values seen similar systems (Figure 28) Diffusion couple studies on the movement of the alloy constituents through a B2 matrix will provide more accurate movement parameters than can be run through PrecipiCalc for more accurate coarsening rates.

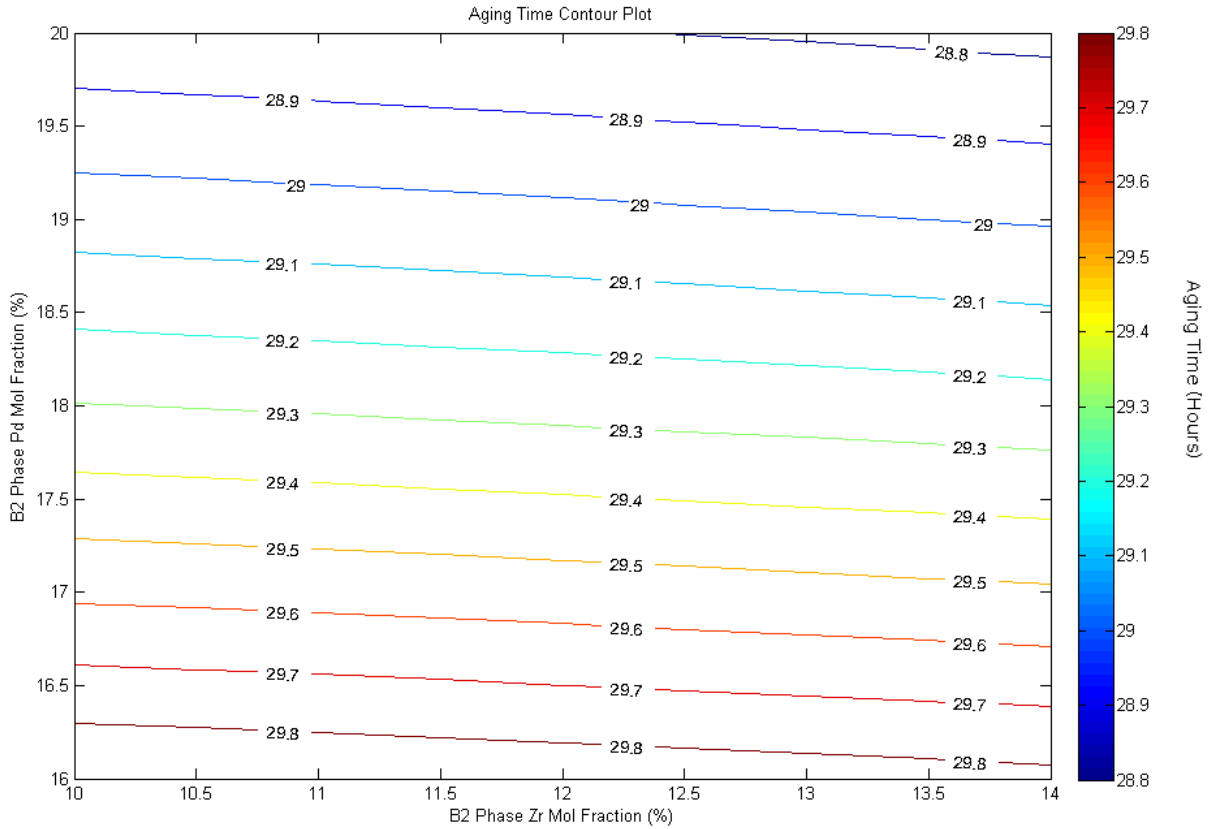


Figure 28: Aging Time Contour Plot

The shear modulus calculations can also be improved through the development of more advanced DFT calculations. Currently, shear moduli are estimated utilizing a representative poisson’s ratio; however, shear moduli can be calculated directly from DFT for different directions. This will remove another element of uncertainty from the calculated K1 plane and ultimately the strength calculations of the alloy.

7 Conclusions

Shape memory alloys are of particular interest due to their use in biomedical applications. An ultra-high cycle fatigue-resistant shape memory alloy was successfully designed using a computational approach. The use of a recently developed Pd-containing thermodynamic database allowed for a more accurate alloy design with low Ni content for improved biocompatibility. The approach taken in this design demonstrates that using computational models can produce a viable solution while decreasing the need for expensive and time-consuming experimental procedures. Innovatively designed shape memory alloys in heart valve frames allow for fewer and less invasive surgeries. This is particularly important for patients who cannot safely undergo open-heart surgery. Optimizing valve performance through the systematic design of a shape memory alloy allows for an improvement in patient quality and length of life.

Although the hybrid alloy that was designed met many of the design objectives, there are still complications in the thermodynamic database used in many of the property calculations. As the database is improved alloys containing more Pd can be explored to improve with biocompatibility even further. This addition of more Pd will lower the yield strength of the alloy, but the current alloy is 500 MPa over the objective so

the goal of 2 GPa may still be met. Advanced DFT calculations and better diffusivity data will also help to model the alloy more effectively. The systematic design approach developed in this alloy design will be fully compatible with the ThermoCalc database as it is improved. Additionally, new processing techniques such as powder metallurgy and yttrium gettering will help to increase the fatigue life of new alloys by limiting void-nucleating inclusions and maintaining a proper ratio of Ni to Ti. Ultimately, this project provides a robust scaffold on which a shape memory alloy can be designed and optimized for biomedical applications that require ultra-high cycle fatigue life.

Appendix A: DFT Code and Calculations

Bash Script:

```
#!/bin/bash
#MSUB -l nodes=32:ppn=2
#MSUB -l walltime=88:00:00
#MPBS -M petersantos2015@northwestern.edu
#MSUB -A t20610
module load espresso/5.0.3
cd $PBS_O_WORKDIR
# Define number of processors
NPROCS='wc -l < $PBS_NODEFILE'
echo "Running on host 'hostname'"
echo "Time is 'date'"
echo "Directory is 'pwd'"
echo "This jobs runs on the following processors:"
echo "'cat $PBS_NODEFILE'"
echo "This job has allocated $NPROCS nodes"
echo ""
echo ""
echo ""
LISTA='11.0 10.95 10.9 10.8 11.21 11.22 11.23 11.24 11.25 11.26 11.27 11.28 11.35 11.45 11.1 11.12 11.14
11.16 11.18 11.2 11.6 11.7'
LISTECUT='160'
LISTK='4'
#####
```

Script to determine the Nickel Titanium Alloy Lattice Constant:

```
for ecut in $LISTECUT
do
for k in $LISTK
```

```

do
for a in $LISTA
do
cat > Ni2TiAl.scf.$a.$ecut.$k.in << EOF
&control
calculation='scf',
restart_mode='from_scratch',
title='Ni2TiAl',
prefix='Ni2TiAl',
pseudo_dir='../pseudo/',
outdir='../tmp/'
/
&system
ibrav=1,
celldm(1)=$a,
nat=16,
ntyp=3,
ecutwfc= $ecut,
ecutrho=720.0,
/
&electrons
conv_thr = 1d-8
/
ATOMIC_SPECIES
Al 26.981539 Al.blyp-n-van_ak.UPF
Ti 47.867 Ti.blyp-sp-van_ak.UPF
Ni 58.6934 Ni.blyp-sp-hgh.UPF

ATOMIC_POSITIONS crystal
Al 0.00000000 0.00000000 0.00000000
Al 0.50000000 0.50000000 0.00000000
Al 0.00000000 0.50000000 0.50000000
Al 0.50000000 0.00000000 0.50000000
Ti 0.50000000 0.00000000 0.00000000
Ti 0.00000000 0.50000000 0.00000000
Ti 0.00000000 0.00000000 0.50000000
Ti 0.50000000 0.50000000 0.50000000
Ni 0.25000000 0.25000000 0.25000000
Ni 0.75000000 0.75000000 0.25000000
Ni 0.75000000 0.25000000 0.75000000
Ni 0.25000000 0.75000000 0.75000000
Ni 0.25000000 0.25000000 0.25000000
Ni 0.75000000 0.25000000 0.25000000
Ni 0.75000000 0.75000000 0.75000000
Ni 0.25000000 0.25000000 0.75000000

```

```

K_POINTS automatic
$k $k $k 1 1 1
EOF
mpirun -machinefile $PBS_NODEFILE -np $NPROCS pw.x <Ni2TiAl6.scf.$a.$ecut.$k.in >
Ni2TiAl_Try6.scf.$a.$ecut.$k.out
done
done
done
# Jiayi setting
#module load espresso/5.0.3
#mpirun pw.x < 806.in > 806.out

```

Appendix B: MATLAB Code and Calculations

```

clc
clear
%Takes composition/parameter inputs
compPd=input('Enter Overall Pd mol fraction ');
compNi=input('Enter Overall Ni mol fraction ');
compTi=input('Enter Overall Ti mol fraction ');
compZr=input('Enter Overall Zr mol fraction ');
compAl=input('Enter Overall Al mol fraction ');
lambda=input('Enter Photon energy in keV ');
phasefraction=input('Enter L21 phase fraction (%)= ');
h21_pd=input('Enter L21 Pd mol fraction ');
h21_zr=input('Enter L21 Zr mol fraction ');
h21_ni=input('Enter L21 Ni mol fraction ');
h21_ti=input('Enter L21 Ti mol fraction ');
h21_al=input('Enter L21 Al mol fraction ');
b2_pd=input('Enter B2 Pd mol fraction ');
b2_zr=input('Enter B2 Zr mol fraction ');
b2_al=input('Enter B2 Al mol fraction ');
b2_ni=input('Enter B2 Ni mol fraction ');
b2_ti=input('Enter B2 Ti mol fraction ');
TCelcius=input('Enter temperature for Lee Coarsening Rate in Celcius ');
% bulk1=ni2tial(GPa)
% bulk2=ni2zral

```

```

% bulk3=pd2tial
bulk1=188.3;
bulk2=251.9;
bulk3=134.9;
v=0.33;
shear1=(3*bulk1*(1-2*v))/(2*(1+v));
shear2=(3*bulk2*(1-2*v))/(2*(1+v));
shear3=(3*bulk3*(1-2*v))/(2*(1+v));
P1=[0,0,shear1];
P2=[0,1,shear2];
P3=[2,0,shear3];
%calculates shear modulus WRT to composition
normal = cross(P1-P2, P1-P3);
planefunction = dot(normal, P1);
ShearMod=-1/normal(3)*[normal(1)*h21_pd/100, normal(2)*h21_zr/100,-planefunction];
ones=[1 1 1];
Gp=dot(ones,ShearMod);
%%%%%%%%%%%%%%%%%%%%%%%%%%%%%%%%%%%%%%%%%%%%%%%%%%%%%%%%%%%%%%%%%%%%%%%%
r=0:0.5:8;
orowan=3.972./r;
k2=(0.019432/10.8)*((Gp-10.8)^(3/2));
normalized_sigma=k2*r;
% plot(r,normalized_sigma)
%
% hold on
%
% plot(r,orowan)
%
% hold off
ropt=sqrt(3.972/k2);
fprintf('Ropt = %d nm \n',ropt)
deltasigma_ss = (2575*((b2_al/100)^0.5))+2730*((0.75*b2_zr/100)^0.5)-(347*0.42*b2_pd/100);
fprintf('deltasigma_ss = %d MPa\n',deltasigma_ss)
f=(phasefraction/100)^0.5;
deltasigma_ppt=f*3.972*1000/ropt;
fprintf('deltasigma_ppt = %d MPa\n',deltasigma_ppt)
deltasigma_y=deltasigma_ppt+deltasigma_ss;

```

```

fprintf('deltastigma_y = %d MPa\n',deltastigma_y)
yield_strength=800+deltastigma_y;
fprintf('yield_strength = %d MPa\n',yield_strength)
mwPd=106.42;
mwNi=59.6934;
mwTi=47.867;
mwZr=91.224;
mwAl=26.9815;
%weight fraction from atomic fraction
totalmass=((compPd*mwPd)+(compNi*mwNi)+(compTi*mwTi)+(compZr*mwZr)+(compAl*mwAl));
wPd=(compPd*mwPd)/totalmass;
wNi=(compNi*mwNi)/totalmass;
wTi=(compTi*mwTi)/totalmass;
wZr=(compZr*mwZr)/totalmass;
wAl=(compAl*mwAl)/totalmass;
%Ni data
EnergyNi=1000.*[1.00E-03 1.00E-03 1.01E-03 1.01E-03 1.50E-03 2.00E-03 3.00E-03 4.00E-03 5.00E-03 6.00E-03
8.00E-03 8.33E-03 8.33E-03 1.00E-02 1.50E-02 2.00E-02 3.00E-02 4.00E-02 5.00E-02 6.00E-02 8.00E-02
1.00E-01 1.50E-01 2.00E-01 3.00E-01 4.00E-01 5.00E-01 6.00E-01 8.00E-01 1.00E+00 1.25E+00 1.50E+00
2.00E+00 3.00E+00 4.00E+00 5.00E+00 6.00E+00 8.00E+00 1.00E+01 1.50E+01 2.00E+01];
murhoNi=[9.86E+03 9.75E+03 9.65E+03 1.10E+04 4.23E+03 2.05E+03 7.09E+02 3.28E+02 1.79E+02
1.09E+02 4.95E+01 4.43E+01 3.29E+02 2.09E+02 7.08E+01 3.22E+01 1.03E+01 4.60E+00 2.47E+00
1.51E+00 7.31E-01 4.44E-01 2.21E-01 1.58E-01 1.15E-01 9.77E-02 8.70E-02 7.94E-02 6.89E-02 6.16E-02
5.49E-02 5.02E-02 4.39E-02 3.75E-02 3.44E-02 3.29E-02 3.21E-02 3.16E-02 3.19E-02 3.32E-02 3.48E-02];
%Pd data
EnergyPd=1000.*[1.00E-03 1.50E-03 2.00E-03 3.00E-03 3.17E-03 3.17E-03 3.25E-03 3.33E-03 3.33E-03 3.46E-03
3.60E-03 3.60E-03 4.00E-03 5.00E-03 6.00E-03 8.00E-03 1.00E-02 1.50E-02 2.00E-02 2.44E-02 2.44E-02
3.00E-02 4.00E-02 5.00E-02 6.00E-02 8.00E-02 1.00E-01 1.50E-01 2.00E-01 3.00E-01 4.00E-01 5.00E-01 6.00E-01
8.00E-01 1.00E+00 1.25E+00 1.50E+00 2.00E+00 3.00E+00 4.00E+00 5.00E+00 6.00E+00 8.00E+00
1.00E+01 1.50E+01 2.00E+01];
murhoPd=[6.54E+03
2.58E+03
1.29E+03
4.73E+02
4.11E+02
1.36E+03
1.29E+03
1.22E+03
1.66E+03
1.52E+03

```

1.38E+03
1.58E+03
1.23E+03
6.91E+02
4.31E+02
2.02E+02
1.11E+02
3.72E+01
1.70E+01
1.00E+01
5.90E+01
3.47E+01
1.61E+01
8.85E+00
5.40E+00
2.48E+00
1.38E+00
5.12E-01
2.83E-01
1.51E-01
1.10E-01
9.13E-02
8.01E-02
6.67E-02
5.85E-02
5.16E-02
4.70E-02
4.16E-02
3.70E-02
3.55E-02
3.52E-02
3.54E-02
3.65E-02
3.80E-02
4.18E-02
4.50E-02]';
%Ti data

EnergyTi=1000.*[1.00E-03

1.50E-03

2.00E-03

3.00E-03

4.00E-03

4.97E-03

4.97E-03

5.00E-03

6.00E-03

8.00E-03

1.00E-02

1.50E-02

2.00E-02

3.00E-02

4.00E-02

5.00E-02

6.00E-02

8.00E-02

1.00E-01

1.50E-01

2.00E-01

3.00E-01

4.00E-01

5.00E-01

6.00E-01

8.00E-01

1.00E+00

1.25E+00

1.50E+00

2.00E+00

3.00E+00

4.00E+00

5.00E+00

6.00E+00

8.00E+00

1.00E+01

1.50E+01

2.00E+01];
murhoTi=[5.87E+03
2.10E+03
9.86E+02
3.32E+02
1.52E+02
8.38E+01
6.88E+02
6.84E+02
4.32E+02
2.02E+02
1.11E+02
3.59E+01
1.59E+01
4.97E+00
2.21E+00
1.21E+00
7.66E-01
4.05E-01
2.72E-01
1.65E-01
1.31E-01
1.04E-01
9.08E-02
8.19E-02
7.53E-02
6.57E-02
5.89E-02
5.26E-02
4.80E-02
4.18E-02
3.51E-02
3.17E-02
2.98E-02
2.87E-02
2.76E-02
2.73E-02

2.76E-02
2.84E-02];
%Al data
EnergyAl=1000.*[1.00E-03
1.50E-03
1.56E-03
1.56E-03
2.00E-03
3.00E-03
4.00E-03
5.00E-03
6.00E-03
8.00E-03
1.00E-02
1.50E-02
2.00E-02
3.00E-02
4.00E-02
5.00E-02
6.00E-02
8.00E-02
1.00E-01
1.50E-01
2.00E-01
3.00E-01
4.00E-01
5.00E-01
6.00E-01
8.00E-01
1.00E+00
1.25E+00
1.50E+00
2.00E+00
3.00E+00
4.00E+00
5.00E+00
6.00E+00

8.00E+00
1.00E+01
1.50E+01
2.00E+01]';
murhoAl=[1.19E+03
4.02E+02
3.62E+02
3.96E+03
2.26E+03
7.88E+02
3.61E+02
1.93E+02
1.15E+02
5.03E+01
2.62E+01
7.96E+00
3.44E+00
1.13E+00
5.69E-01
3.68E-01
2.78E-01
2.02E-01
1.70E-01
1.38E-01
1.22E-01
1.04E-01
9.28E-02
8.45E-02
7.80E-02
6.84E-02
6.15E-02
5.50E-02
5.01E-02
4.32E-02
3.54E-02
3.11E-02
2.84E-02

2.66E-02
2.44E-02
2.32E-02
2.20E-02
2.17E-02];
%Zr data
EnergyZr=1000.*[1.00E-03
1.50E-03
2.00E-03
2.22E-03
2.22E-03
2.26E-03
2.31E-03
2.31E-03
2.42E-03
2.53E-03
2.53E-03
3.00E-03
4.00E-03
5.00E-03
6.00E-03
8.00E-03
1.00E-02
1.50E-02
1.80E-02
1.80E-02
2.00E-02
3.00E-02
4.00E-02
5.00E-02
6.00E-02
8.00E-02
1.00E-01
1.50E-01
2.00E-01
3.00E-01
4.00E-01

5.00E-01
6.00E-01
8.00E-01
1.00E+00
1.25E+00
1.50E+00
2.00E+00
3.00E+00
4.00E+00
5.00E+00
6.00E+00
8.00E+00
1.00E+01
1.50E+01
2.00E+01]';
murhoZr=[4.21E+03
1.63E+03
8.12E+02
6.26E+02
2.39E+03
2.24E+03
2.12E+03
2.95E+03
2.64E+03
2.36E+03
2.69E+03
1.77E+03
8.51E+02
4.76E+02
2.94E+02
1.36E+02
7.42E+01
2.46E+01
1.50E+01
9.47E+01
7.24E+01
2.49E+01

```

1.14E+01
6.17E+00
3.74E+00
1.72E+00
9.66E-01
3.79E-01
2.24E-01
1.32E-01
1.02E-01
8.69E-02
7.76E-02
6.57E-02
5.81E-02
5.15E-02
4.70E-02
4.15E-02
3.64E-02
3.45E-02
3.38E-02
3.37E-02
3.44E-02
3.55E-02
3.86E-02
4.12E-02]';
%find the energy closest to lambda for each element
for i=1:numel(EnergyPd)
if EnergyPd(i)-lambda<=0.001
MuRhoPdchoose=muRhoPd(i);
end
end
for i=1:numel(EnergyNi)
if EnergyNi(i)-lambda<=0.001
MuRhoNichoose=muRhoNi(i);
end
end
for i=1:numel(EnergyTi)
if EnergyTi(i)-lambda<=0.001

```

```

MuRhoTichoose=murhoTi(i);
end
end
for i=1:numel(EnergyAl)
if EnergyAl(i)-lambda<=0.001
MuRhoAlchoose=murhoAl(i);
end
end
for i=1:numel(EnergyZr)
if EnergyZr(i)-lambda<=0.001
MuRhoZrchoose=murhoZr(i);
end
end
%calculate weighted mass attenuation coefficient
massattcoeff=(wPd*MuRhoPdchoose)+(wNi*MuRhoNichoos)+ (wTi*MuRhoTichoose)+(wZr*MuRhoZrchoose)+(wAl*Mu
fprintf('mu/rho = %f cm^2/g \n',massattcoeff);
omega_h21=(h21_pd*8.56)+(h21_zr*13.81)+(h21_ni*6.59)+(h21_ti*10.62)+(h21_al*10);
omega_b2=(b2_pd*8.56)+(b2_zr*13.81)+(b2_ni*6.59)+(b2_ti*10.62)+(b2_al*10);
misfit=abs((((omega_h21/omega_b2)^(1/3))-1)*100));
fprintf('misfit = %d percent \n',misfit)
%%%%%%%%%%%%%%%%%%%%%%%%%%%%%%%%%%%%%%%%%%%%%%%%%%%%%%%%%%%%%%%%%%%%%%%%
TiPd=591;
TiNi=89;
AlPd=-2272.32;
AlNi=-7245;
ZrPd=245.356;
ZrNi=1217.25;
LONiPd_Ti=-720.43;
L1NiPd_Ti=-507.46;
LONi_ZrTi=-919.32;
PdC=b2_pd;
ZrC=b2_zr;
NiC=b2_ni;
Ti2C=b2_ti;
Al2C=b2_al;
Af=(TiPd.*PdC/50.*Ti2C/50)...
+(TiNi.*NiC/50.*Ti2C/50)...

```

```

+(AlPd.*PdC/50.*b2_al./50)...
+(AlNi.*NiC/50.*b2_al./50)...
+(ZrPd.*PdC/50.*b2_zr./50)...
+(ZrNi.*NiC/50.*b2_zr./50)...
+(L0Ni_ZrTi.*NiC/50.*Ti2C/50.*b2_zr./50)...
+(L0NiPd_Ti.*NiC/50.*PdC/50.*Ti2C/50)...
+(L1NiPd_Ti.*NiC/50.*PdC/50.*Ti2C/50.*(NiC/50-PdC/50)-403.*(phasefraction/100));
fprintf('Af = %d (C) \n',Af)
%%%%%%%%%%%%%%%%%%%%%%%%%%%%%%%%%%%%%%%%%%%%%%%%%%%%%%%%%%%%%%%%%%%%%%%%%%%%%%
% Calculate Coarsening Rate
% Ti is component 1
% <r>^3-<ro>^3=(4/9)*K*t
% assume <ro>^3=0
% Ki=xibeta/xialpha
sigma=0.0603; %J/m^2 (interfacial energy, from Bender thesis)
Vmbeta=(h21_pd./100*8.851E-6)+(h21_zr./100*14.01E-6)+(h21_ni./100*6.589E-6)+(h21_ti./100*10.62E-6)+(h21_al./100*10E-6);
T=TCelcius+273.15;
kTi=h21_ti/b2_ti;
kNi=h21_ni/b2_ni;
kAl=h21_al/b2_al;
kZr=h21_zr/b2_zr;
kPd=h21_pd/b2_pd;
%Dmalpha (diffusivity in B2 matrix (m^2/s), at 600C)
DZr=2.9093e-10;
DPd=6.0144E-19;
DAI=8.895E-19;
DNi=1.346E-17;
DTi=1.4695E-19;
%Bracket Part for Ti
TiPart=((kTi-kTi)*(kTi-1)*(b2_ti/DTi));
NiPart=((kNi-kTi)*(kNi-1)*(b2_ni/DNi));
ZrPart=((kZr-kTi)*(kZr-1)*(b2_zr/DZr));
AlPart=((kAl-kTi)*(kAl-1)*(b2_al/DAI));
PdPart=((kPd-kTi)*(kPd-1)*(b2_pd/DPd));
K=((2*sigma*Vmbeta)/(8.314*T))*(TiPart+NiPart+ZrPart+AlPart+PdPart)^(-1);
agingtime=((9/4)*((ropt*(10^-9))^3)/K)/3600;

```

```

fprintf('K Lee Coarsening Rate = %d \n',K)
fprintf('Aging Time = %d (hours) \n',agingtime)
%%%%%%%%%%%%%%%%%%%%%%%%%%%%%%%%%%%%%%%%%%%%%%%%%%%%%%%%%%%%%%%%%%%%%%%%
%Calculate Energy Shift
%Sigma plane is fit from 3 experimental data points
sigma = -11.11.*h21_pd/100 - 229.73.*h21_zr/100 +201; %mJ/m^2
sigma = sigma./1000; %converting to J/m^2
%E_corr plane is fit from 3 experimental data points
E_corr = -1770.37.*h21_pd/100 + 6318.92.*h21_zr/100 +138; %J/mol
r_opt=ropt.*10^-9;
E_cap = Vmbeta.*2.*sigma./r_opt;
E_shift = E_cap + E_corr;
fprintf('Energy Correction = %d (J/mol) \n',E_shift)

```

References

- [1] Lorenza Petrini and Francesco Migliavacca. Biomedical applications of shape memory alloys. *Journal of Metallurgy*, 2011(Article ID 501483):15 pages, 2011.
- [2] E. Engmann and M.R. Asch. Clinical experience with the antecubital simon nitinol IVC filter. *Journal of Vascular and Interventional Radiology*, 9(5):774–778, 1998.
- [3] E. Bruckheimer, A.G. Judelman, S.D. Bruckheimer, I. Tavori, G. Naor, and B.T. Katzen. In vitro evaluation of a retrievable low-profile nitinol vena cava filter. *Journal of Vascular and Interventional Radiology*, 14(4):469–474, 2003.
- [4] G. Lewis. Materials, fluid dynamics, and solid mechanics aspects of coronary artery stents: a state-of-the-art review. *Journal of Biomedical Materials Research*, 86(2):569–590, 2008.
- [5] K.P. Walsh and I.M. Maadi. The amplatzer septal occluder. *Cardiology in the Young*, 10(5):493–501, 2000.
- [6] L. Coats and P. Bonhoeffer. New percutaneous treatments for valve disease. *Heart*, 93(5):639–644, 2007.
- [7] J.C. Laborde, D.V.M. Borensyein, D.V.M. Behr, B. Farah, and J. Fajadet. Percutaneous implantation of the corevalve aortic valve prosthesis for patients presenting high risk for surgical valve replacement. *Eurointerv*, 1(472-474):2006.
- [8] G. Song, N. Ma, and H.N. Li. *Engineering Structures*, 28:1266–1274, 2006.
- [9] J. Mohd Jani, M. Leary, A. Subic, and M.A. Gibson. *Materials & Design*, 56:1078–1113, 2014.
- [10] K. Otsuka and C.M. Wayman. *Shape Memory Materials*, 1999.
- [11] G. Kauffman and L. Mayo. *Chemical Matters*, pages 4–7, 1993.
- [12] A. Coda, S. Zillo, D. Norwich, and F. Sczerzenie. Characterization of inclusions in VIM/VAR NiTi alloys. *Journal of Materials Engineering Performance*, 21:2572–2577, 2012.
- [13] F. Sczerzenie, G. Vergani, and C. Belden. The measurement of total inclusion content in nickel titanium alloys. *Journal of Materials Engineering and Performance*, 21:2578–2586, 2012.
- [14] M. Elahinia, M. Tabesh, M. Hashemi, and S. Bhaduri. Manufacturing and processing of TiNi implants: A review. *University of Toledo*.
- [15] A. Toro, F. Zhou, M.H. Wu, W. Geertruyden, and W.Z. Misiolek. Characterization of non-metallic inclusions in superelastic NiTi tubes. *Journal of Materials Engineering and Performance*, 18:448–458, 2009.
- [16] J.M. Gallardo Fuentes, P. Gümpel, and J. Strittmatter. Phase change behavior of nitinol shape memory alloys. *Advanced Engineering Materials*, 4:437–451, 2002.
- [17] G. Eggeler, E. Hornbogen, A. Yawny, A. Heckman, and M. Wagner. Structural and functional fatigue of NiTi shape memory alloys. *Materials Science and Engineering*, 378:24–33, 2004.
- [18] M. Bender and G.B. Olson. Designing a precipitation-strengthened, superelastic, TiNi-Based alloy for endovascular stents. *ICOMAT*, pages 159–166.
- [19] P.H. Adler, J. Allen, J. Lessar, and R. Francis. *Journal of ASTM International*, 4(7):1–16, 2007.
- [20] K. Gall, J. Tyber, G. Wilkesanders, S.W. Robertson, R.O. Ritchie, and H.J. Maier. Effect of microstructure on the fatigue of hot-rolled and cold-drawn NiTi shape memory alloys. *Materials Science and Engineering: A Structural Materials: Properties, Microstructure and Processing*, 486(1-2):389–403.

- [21] J. Jung, G. Ghosh, and G.B. Olson. A comparative study of precipitation behavior of heusler phase (Ni₂TiAl) from b2-TiNi in ni-ti-al and ni-ti-al-x (x= hf, pd, pt, zr) alloys. *Acta Materialia*, 51(20):6341–6357, 2003.
- [22] Y. Kozumi, Y. Ro, S. Nakazawa, and H. Harada. NiTi-base intermetallic alloys strengthened by al substitution. *Materials Science and Engineering: A Structural Materials: Properties, Microstructure and Processing*, 223(1-2):36–41, 1997.
- [23] M.D. Ph.D. Bender. *Dissertation*. PhD thesis, Northwestern University, 2008.
- [24] M.N. Helmus, D.F. Gibbons, and D. Cebon. Biocompatibility: Meeting a key functional requirement of next-generation medical devices. *Toxicologic Pathology*, 36:70–80, 2008.
- [25] M.N. Helmus. *Biomaterials in the design and reliability of medical device*. Kluwer Academic/Plenum Publishers and Landes Bioscience, New York and Georgetown, TX, 2003.
- [26] M. Es-Souni, M. Es-Souni, and H. Fischer Brandies. Assessing the biocompatibility of NiTi shape memory alloys used for medical applications. *Analytical and Bioanalytical Chemistry*, 381(3):557–567, 2005.
- [27] M.D. Bender. *Computational Design of Precipitation-strengthened Titanium-nickel-based Shape Memory Alloys*. ProQuest, 2008.
- [28] NIST US Department of Commerce. NIST: x-ray mass attenuation coefficients.
- [29] G.A. Jenkins. The systems approach. *Systems Behavior*, page 56, 1972.
- [30] C.S. Smith. *A Search for Structure*. MIT Press, Cambridge, MA, 1981.
- [31] G.B. Olson. Computational design of hierarchically structured materials. *Science*, 277:1237–1242, 1997.
- [32] G.B. Olson. Overview: Science of steel. pages 3–66. Government Printing Office, Washington, D.C., 1990.
- [33] H.A. Roth, C.L. Davis, and R.C. Thompson. Modeling solid solution strengthening in nickel alloys. *Metallurgical and Materials Transactions A*, 28:1329–1335, 1997.
- [34] J.W. Ph.D. Jung. *Dissertation*. PhD thesis, Northwestern University, 2003.
- [35] G.S. Bigelow, S.A. Padula, A. Garg, and R.D. Noebe. Correlation between mechanical behavior and actuator-type performance of ni-ti-pd high-temperature shape memory alloys. *Behavior and Mechanics of Multifunctional and Composite Materials*, 65(26):247–255, 2007.
- [36] C. Poupard, K. Jin, S.C. Yoo, and C. Kadleck. Team shape memory. Technical report, Northwestern University, 2012.
- [37] T. Ph.D. Jiang. *Dissertation*. PhD thesis, Northwestern University, 2012.
- [38] T.H. Courtney. *Mechanical behavior of materials*, 2005.
- [39] A. Melander and P.A. Persson. The strength of a precipitation hardened AlZnMg alloy. *Acta Metallurgica*, 26(2):267–278, 1978.
- [40] Particle strengthening. In *Plastic Deformation and Fracture of Materials*, pages 312–357. Wiley, Weinheim, Germany, 1992.
- [41] W. Huther and B Reppich. Interaction of dislocations with coherent, stress-free, ordered particles. *Z. Metallk*, 69:628–634, 1978.
- [42] L. M. Brown, R. H. Cook, R. K. Ham, and G. R. Purdy. Elastic stabilization of arrays of precipitates. 7(8):815–820.

- [43] S. F Hsieh and S. K Wu. Room-temperature phases observed in Ti₅₃-xNi₄₇Zr_x high-temperature shape memory alloys. *Journal of Alloys and Compounds*, 266(1–2):276–282, February 1998.
- [44] K. Batalovic, V. Kotesi, and D. Stojic. *Journal of Physical Chemistry*, 117:26914–26920, 2013.
- [45] P. Ravindran, L. Fast, P.A. Korzhavyi, B. Johansson, J. Wills, and O. Eriksson. *Journal of Applied Physics*, 84:4891–4904, 1998.
- [46] Sergiy V. Divinski, Ivo Stloukal, Lubomir Kral, and Christian Herzig. Diffusion of titanium and nickel in b2 NiTi. *Defect and Diffusion Forum*, 289-292:377–382, April 2009.
- [47] D.A. Porter, K.E. Easterling, and M.Y. Sherif. *Phase Transformations in Metals and Alloys*. CRC Press: Taylor & Francis Group, LLC, United Kingdom, 3 edition, 2009.
- [48] D. Frankel. *Qualifier*. PhD thesis, Northwestern University, 2012.
- [49] O.W. Linton. Medical applications of x-rays. *Beam Line*, (Summer):25–34, 1995.
- [50] M.H. Wu. Fabrication of nitinol materials and components. Technical report, Memry Corporation, Kunming, China, 2001.
- [51] Akira Terayama, Koji Nagai, and Hideki Kyogoku. Fabrication of ti-ni-zr shape memory alloy by P/M process. *Materials Transactions*, 50(10):2446–2450, 2009.
- [52] S. K. Sadrnezhaad and A. R. Selahi. Effect of mechanical alloying and sintering on Ni–Ti powders. *Materials & Manufacturing Processes*, 19(3):475 – 486, 2004.
- [53] F. J. Gil, J. M. Manero, and J. A. Planell. Effect of grain size on the martensitic transformation in NiTi alloy. *Journal of Materials Science*, 30(10):2526–2530, May 1995.
- [54] J. Tran. *Dissertation*. PhD thesis, Northwestern University, 2009.
- [55] B. Bertheville. Powder metallurgical processing of ternary Ni₅₀Ti₅₀-xZr_x (x = 5, 10 at.%) alloys. *Journal of Alloys and Compounds*, 398(1–2):94–99, August 2005.
- [56] M. Yan, Y. Liu, Y. B. Liu, C. Kong, G. B. Schaffer, and M. Qian. Simultaneous gettering of oxygen and chlorine and homogenization of the β phase by rare earth hydride additions to a powder metallurgy Ti–2.25Mo–1.5Fe alloy. *Scripta Materialia*, 67(5):491–494, September 2012.
- [57] Nagaiyar Krishnamurthy and Chiranjib Kumar Gupta. *Extractive Metallurgy of Rare Earths*. CRC Press, December 2004.
- [58] M. Yan, Y. Liu, G. B. Schaffer, and M. Qian. In situ synchrotron radiation to understand the pathways for the scavenging of oxygen in commercially pure ti and Ti–6Al–4V by yttrium hydride. *Scripta Materialia*, 68(1):63–66, January 2013.
- [59] Xiu Song, Mitsuo Niinomi, Masaaki Nakai, Harumi Tsutsumi, and Lei Wang. Improvement in fatigue strength while keeping low young’s modulus of a β -type titanium alloy through yttrium oxide dispersion. *Materials Science and Engineering: C*, 32(3):542–549, April 2012.
- [60] P. Gianozzi, S. Baroni, N. Bonini, M. Calandra, R. Car, C. Cavazzoni, D. Ceresoli, G.L. Chiaroti, M. Cococcioni, I. Dabo, A.D. Corso, S. de Gironcoli, S. Fabris, G. Fratesi, R. Gebauer, U. Gerstmann, C. Gougoussis, A. Kokali, M. Lazzeri, L. Martin-Samos, N. Marzari, F. Mauri, R. Mazzarello, S. Paolini, A. Pasquarello, L. Paulatto, C. Sbraccia, S. Scandolo, G. Sclauzero, A.P. Seitsonen, A. Smogunov, P. Umari, and R.M. Wentzcovitch. QUANTUM ESPRESSO: a modular open-source software project for quantum simulations of materials. 21:395–502.
- [61] David Groh, Ravindra Pandey, Munima B. Sahariah, Emilie Amzallag, Isabelle Baraille, and Michel Rérat. First-principles study of the optical properties of BeO in its ambient and high-pressure phases. 70(5):789–795.

- [62] X. Yan, A. Grytsiv, P. Rogl, V. Pomjakushin, and M. Palm. *J Phys Equil and Diff*, 29:500–508, 2008.
- [63] K.R.A. Ziebeck and K.U. Neumann. *Alloys and Compounds of d-Elements with Main Group Elements. Part 2*. Landolt-Bornstein, Berlin Heidelberg, 2001.
- [64] K.U. Neumann, J. Crangle, J.G. Smith, N.K. Zayer, and K.R.A. Ziebeck. *Journal of Magnetism and Magnetic Materials*, 137:264–268, 1994.